Article:

Qi, R., Langdon, G.S., Cloete, T.J. et al. (2020) Behaviour of a blast-driven ball bearing embedded in rear detonated cylindrical explosive. International Journal of Impact Engineering, 146. 103698. ISSN: 0734-743X

https://doi.org/10.1016/j.ijimpeng.2020.103698

Behaviour of a blast-driven ball bearing embedded in rear detonated cylindrical explosive

R. Qi[1], G.S. Langdon[1,2], T.J. Cloete[1], S. Chung Kim Yuen[1]

[1]*Blast and Impact Survivability Research Unit (BISRU), Department of Mechanical Engineering, University of Cape Town, Rondebosch, 7700, South Africa.*

[2]*Department of Civil and Structural Engineering, University of Sheffield, Sheffield, S13JD, UK.*

Abstract

This paper presents insights into the flight characteristics of a ball bearing embedded in a rear detonated cylindrical charge, which represents an idealised piece of shrapnel from an improvised explosive device. A novel experimental technique was developed to quantify the loading from a blast-driven ball bearing. The impulse contributions from the blast pressure and the ball bearing impact were separately identifiable in the experimental data. Computational simulations, validated using experimental data, were used to elucidate additional detail about the momentum transfer and damage in the ball bearings during the blast event. The results show the critical influence of charge mass and aspect ratio on the development of the detonation pressure profile, its interaction with the embedded bearing, and the flight characteristics of the bearing. Length-to-diameter ratios below a critical value were more efficient in transferring momentum to the embedded bearings. These findings provide unique and detailed insights that will prove valuable to blast protection engineers considering the effects of embedded projectiles in improvised explosive devices.

1. Introduction

Between 2011 and 2016, over 130 000 people [1] were injured or died during incidents involving improvised explosive devices (IED), 81% of whom were innocent civilians. IEDs remain a threat to the safety of the general public. As the name 'IED' suggests, this type of explosive weapon is improvised (often home-made) and can take many forms or shapes. In many cases, the explosives are embedded with other household items (such as nails or ball bearings) to enhance their lethality. One of the great difficulties in IED research is the wide variety of possible configurations. Hence, a fundamental understanding of the momentum transfer mechanisms to embedded solid particles in the explosive is needed. This will allow model validation at the fundamental level so that more complex models representing real IEDs can be developed with confidence.

The two simplest explosive charge shapes to model are spheres and cylinders, due to their symmetry. While spherical shaped explosives are simpler, the cylindrical charge shape is a more realistic and practical option for an IED (for example, pipe bombs). Additionally, most ordnance and warheads are basically cylindrical. Considerable work has examined the shock wave and impulse distributions resulting from the detonation of cylindrical charges [2-12]. Most work compares the development to that of spherical charge detonations. The effect of charge shape was found to be most significant in the near field, and of decreasing importance at longer stand-off distances. The Hopkinson-Cranz scaled distance, Z is given by the expression $R/W^{1/3}$, where R is the stand-off distance from the charge to the target and W is the TNT equivalent charge mass. For $Z > 5$ m/kg$^{1/3}$, the effect of charge shape on peak pressure was insignificant [2]. Similarly, Held [3] investigated the impulse distribution from cylindrical charges by tracking the displacement of metal cylinders. The radial impulse distribution was found to be distinctively different from that of a spherical charge. Rigby et al [4] measured the impulse distribution arising from the detonation of spherical and cylindrical charges. The work showed that cylindrical charges with a 1/3 length/diameter (*L*/*D*) aspect ratio produced similar axial impulse distributions on the target plates as spheres with a much smaller charge mass.

Ismail and Murray [5] showed that a cylindrical charge generates complex blast waves, comprising multiple reflections. Spherical waves are generated in both the axial (end) and radial (side) directions, and these waves interact and constructively interfere [6]. The overlapping waves form a bridge wave reinforced by both the axial and radial waves. The distribution of pressure and impulse is extremely non-uniform, particularly in the near-field, demonstrated by Wu et al [7, 8] when filming the fireball generated by an rear-detonated cylinder of Composition B. Xiao et al [9] reported results from a numerical study into the influence of detonation point and aspect ratio on the pressure and impulse characteristics of cylindrical TNT charges. Higher pressures were evident when the cylinders were detonated from one end, but the effect of shape could be neglected when $Z >$ 3.9 m/kg$^{1/3}$ for both overpressure and impulse magnitude. In the near-field (at $Z = 0.7$ m/kg$^{1/3}$), the shock wave was highly focused in the axial direction with pressure up to four times that predicted for the same mass spherical charge.

The influence of charge aspect ratio (*L*/*D*=0.0262 to *L*/*D*=0.477) and charge diameter on axial impulse was investigated using ballistic pendula in ref [10-12]. The axial impulse increased with increasing in charge diameter for a given charge mass. The charge aspect (*L*/*D*) ratio significantly influences the blast load distribution, with less energy in the axial direction at higher *L*/*D* ratios [6-12]. Kennedy [13] reported that the axial impulse from cylindrical charges varied considerably with the charge aspect ratio, as they are subject to side losses. Thus, the effective volume of a cylindrical charge was limited to the shape of a cone. A critical aspect ratio $L/D = \sqrt{3}/2$ was suggested to be the maximum effective aspect ratio for axial impulse.

Whilst there is a large body of literature on cratering damage due to impact, research into blast-induced projectile impacts are focused on fragmentation [14-17], such as that in warhead, or blast driven metal [13]. A limited experimental study on the damage caused by incorporating a foreign object in an explosive charge is available in reference [18]. Kang and Chung Kim Yuen [18] did not measure the velocity of the explosively driven projectiles, but analysed the damage distribution in the walls of a surrounding steel cylinder. They used the penetration depth to infer information about the effect of packing pattern.

This paper reports the results of experimental and numerical studies on the influence of cylindrical charge geometry on the velocity characteristics of an explosively driven single ball bearing. The paper provides detailed insights into the flight characteristics of a ball bearing embedded in a rear detonated cylindrical charge, which is of enormous practical relevance to IED research. Charge mass and aspect ratio are both considered. The paper is arranged as follows. The explosive charge design and experimental arrangement are described in sections 2 and 3 respectively. Section 4 reports the results of the blast tests while section 5 describes the computational modelling approach. The axial impulse, ball bearing flight velocities and bearing damage are discussed, using the experimental and simulation results. Finally, the performance of the experimental arrangement, the verdict on the influence of charge geometry on the ball bearing velocity is presented in conclusions.

2. Simplified explosive charge design

A cylindrical charge shape is used to represent an IED in one of its simplest forms. IEDs come in a range of shapes and sizes, from hand-held to vehicle borne, and it is impossible to reproduce the full range of possibilities in the laboratory. Most have some embedded particles, which in this work have been simplified to one spherical ball embedded in a rear detonated cylindrical charge. As shown in Figure 1, this simple representation comprised an unconfined, rear detonated cylindrical charge of variable length (L) and diameter (D), with a single Ø 5 mm ball bearing that was half-buried on the front face. Rear detonated cylindrical charges have been shown to generate the highest axial impulses and pressures [9], meaning that they would be expected to produce the highest ball bearing velocities (therefore a worst-case scenario for an IED threat). The bearing was half-buried to allow certainty about the contact area between the ball bearing and the explosive and to ensure good contact them during the experiments. The sphericity of the ball bearings was measured prior to testing and it was found to deviate by less than 1 μm. The mean mass of the ball bearings was found to be 0.505 g.

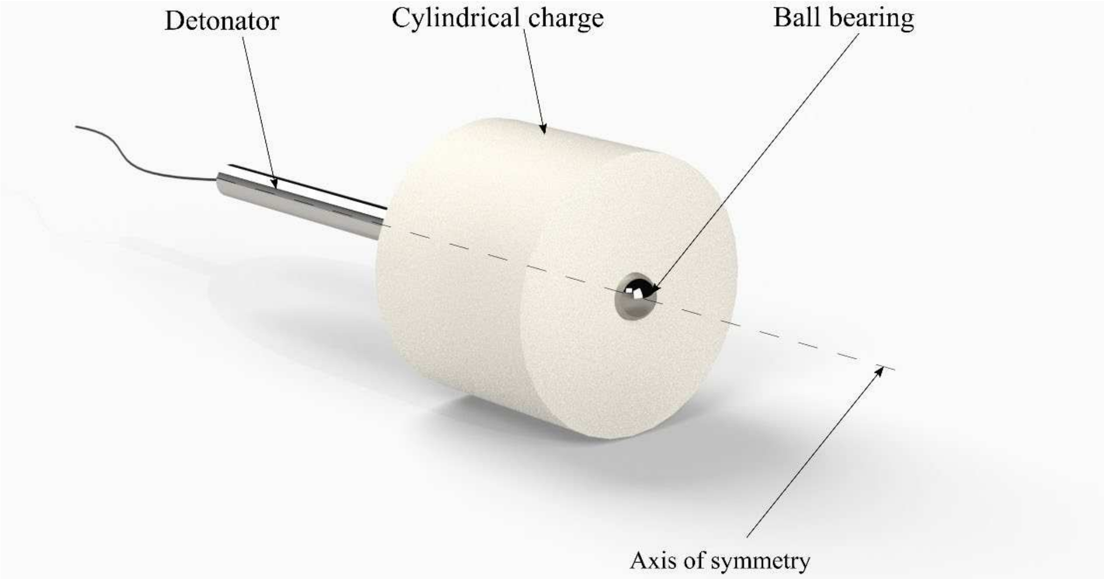

Figure 1: Schematic showing a rear-detonated PE4 explosive charge with a ball bearing embedded in the front surface

The arrangement used in previous research into explosively driven metal [14-15] included metal that either covered the entire face of the charge or encapsulated the entire charge. In this work, none of the charge was encased, thus the effects of confinement were removed, allowing the charge geometry influence to be isolated. The influence of charge geometric parameters, such as the aspect ratio (*L/D*) and the charge diameter on the one-dimensional velocity of the ball bearing was investigated both numerically and experimentally.

3. Experimentation

3.1 Blast test arrangement

Blast tests involved detonating cylindrical charges (2.2 g to 27.2 g PE4 plastic explosive) at the open end of a 100 mm long blast tube, as shown in Figure 2. The blast tube was employed primarily for safety reasons to address concern about damage should the high-speed ball bearing veer off course. Additionally, the tube enables confidence that the impulse inferred from the pendulum swing was all applied to the witness plates and not as a result of reflections from nearby surfaces. The charge mass, diameter and length of the cylindrical charge was varied. A single ball bearing was embedded to half height in the top of each charge at the radial centre, while the detonator was attached at the radial centre of the rear face, as described above. The blast tube was mounted onto a single degree of freedom horizontal pendulum. The pendulum impulse was obtained by tracking the pendulum motion using a laser displacement sensor, similar to Curry and Langdon [19].

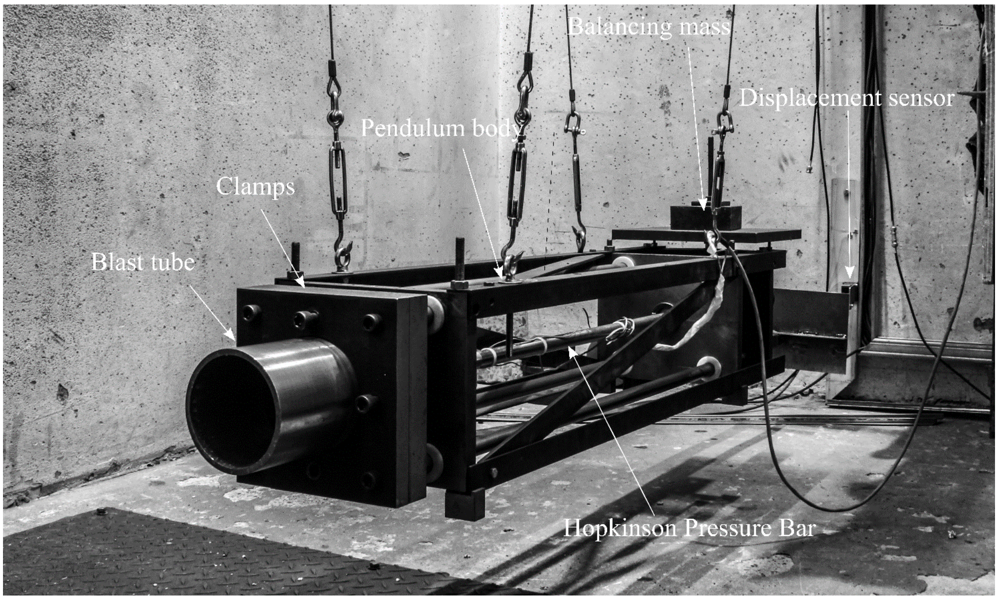

Figure 2: Photograph of the blast experimental arrangement

The experimental arrangement was designed to record the ball bearing velocity after detonation. Optical techniques were not suitable due to the presence of fireballs and shock fronts that obscure the ball bearing in flight. Additionally, the small size of the ball bearing made it difficult for optical equipment to track and focus. Therefore, two alternative methods were used to infer ball bearing velocity:

- recording of flight duration of the projectile over a known distance (average velocity)
- correlating projectile impact velocity with the impact crater depth (impact velocity)

Table 1 A summary of the tensile test results of the witness plate material (average of four experiments).

		0.2% Proof Strength (MPa)	Ultimate Tensile Strength (MPa)
Tested result	Mean	298.9	355.2
	Standard deviation	2.9	1.9
Specification from manufacturer [18]	Minimum	255	295
	Maximum	315	330

A photograph of the modified ballistic pendulum arrangement is shown in Figure 2. A centrally located Hopkinson Pressure Bar (HPB) was used to record the time of impact. A pair of witness plates (inner and outer) were placed in front of the HPB. The witness plate assembly was used to capture the cratering characteristics of the ball bearing; the crater depth was used to infer the impact velocity. The outer witness plate was supported by a steel plate and the inner plate was supported by the HPB. This arrangement enabled the tracking of average and impact velocity of the ball bearing as well as the force history and impulse of the detonation. The inner witness plate had the same diameter as the HPB and was designed to slide with minimum friction. Both witness plates were manufactured from Al6082-T6 aluminium alloy round bar. Quasi-static tensile tests were conducted, at a nominal strain rate of $10^{-3}s^{-1}$, using the DIN EN 10002-1 standard [20]. The 0.2 % proof strength and ultimate tensile strength are shown in Table 1, after correcting for machine compliance, alongside the manufacturer's data [21].

3.2 Shaping and aligning the explosive charge

Expanded polystyrene (EPS) pads have been used previously [10-12] to position the explosive and the detonator before detonation. Jacob et al [22] showed that the effect of EPS on impulse decreased with the increase in standoff distance (SOD). Improvements were needed for near-field blast arrangements, so Davids et al [23] replaced the thin EPS pad with an EPS bridge arrangement. This positioned the EPS behind the charge (rather than in between the charge and the target), minimising its influence on the load.

In this work, the influence of EPS was further reduced by designing an EPS bridge that directed blast pressure away from the charge. This was necessary as unconfined charges are extremely sensitive to the orientation and the position of the detonator [6], especially when being used to accelerate (imparting impulse to) a small, lightweight projectile located at the radial centre of the cylindrical charge face. Blast wave reflections could create asymmetry in the ball bearing loading, causing it to deviate in flight, missing the centre of the HPB. Thus, a new the EPS bridge was designed, incorporating V-shaped beams as shown in Figure 3, to deflect axial and radial blast waves away from the ball. The two side bridges fitted into the main bridge that held the charge and the detonator. All parts were hot-wire cut to ensure surface smoothness. An undersized central hole ensured the detonator remained in the correct position.

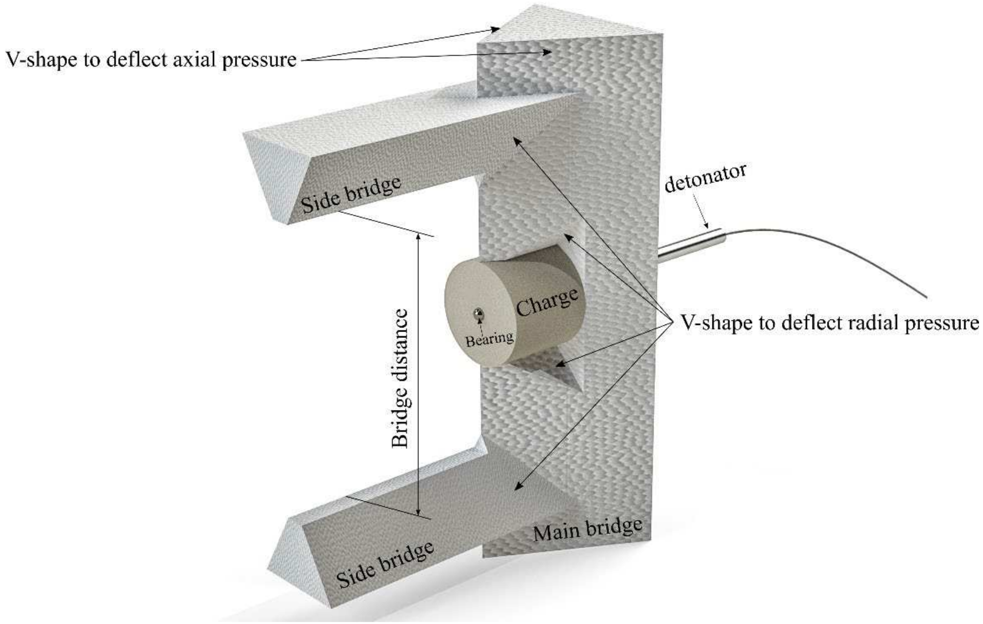

Figure 3: Schematic showing the EPS bridge used to position and charge

A split mould, machined from polytetrafluoroethylene (PTFE) was used to ensure the consistency and accuracy in charge shape and the ball bearing placement. A detailed description of this can be found in ref [28].

3.3 The Hopkinson pressure bar (HPB) arrangement

The HPB was a 1 m long silver steel, 20 mm diameter, round bar. This length enabled the stress waves from the pressure and impact event to be recorded without the interference caused by the reflected signal. Two pairs of double-eccentric bushings were used to align the HPB. Further details about the HPB including the strain gauge configurations can be obtained from Cloete et al [24-25].

The axial impulse captured by the HPB was calculated by the summation of pressure over time and area as shown in Equation 1. Where A_{bar} is the area of the HPB across the blasted face, t_b is the first blast arrival time, Δbar is the duration for the first blast signal to reflect, t_{i_0} and t_{i_1} are the initial and final time of the impact event.

$$I_{HPB} = \left(\sum_{t=t_b}^{t_b+\Delta bar} p(t) - \sum_{t=t_{i_0}}^{t_{i_1}} p(t) \right) A_{bar} \qquad 1$$

An example of the impact and blast pressure history is shown in Figure 4. The two more prominent pressure peaks were attributed to the initial blast pressure and the impact of the ball bearing. As shown in Equation 1, the impulse recorded during the impact was removed from the total impulse. This method assumed that the impulse from blast loading was negligible during the impact event.

Negative signals shown in Figure 4 were regarded as background electromagnetic (EM) noise as it was physically impossible given the loading condition. The distribution of EM noises were expected to be random, therefore the negative and positive EM noises should have an error cancelling effect through summation using Equation 1.

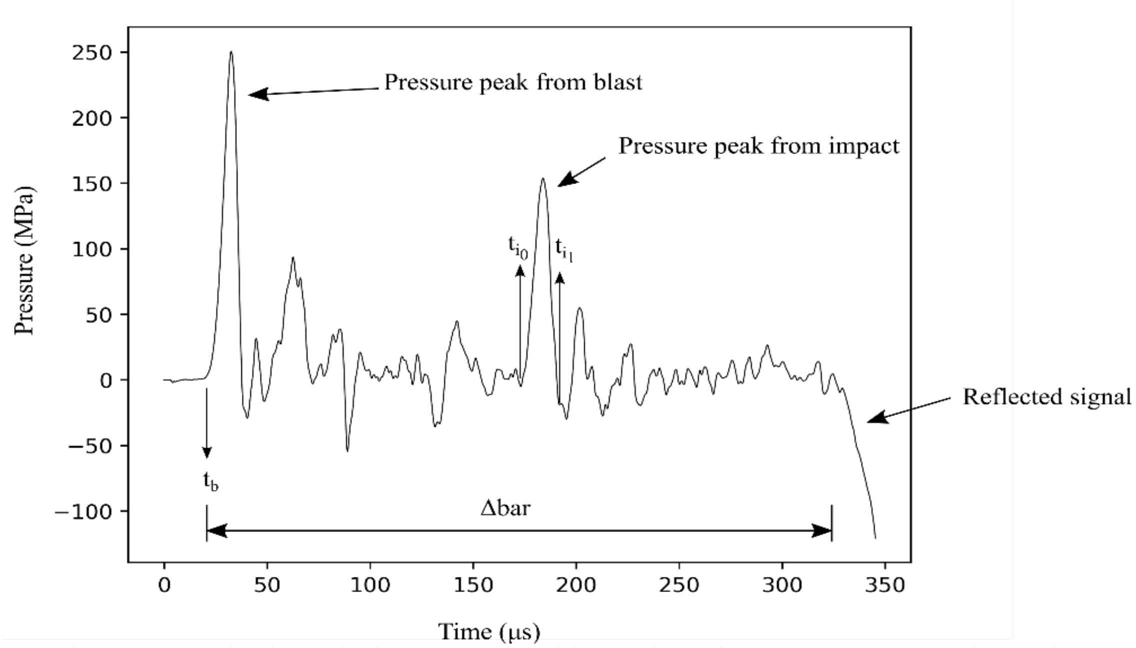

Figure 4: Graph of a typical pressure-time history from the HPB (10.4 g PE4 detonation)

3.4 Velocity calculations

3.4.1 Average in-flight velocity of the ball bearing

The time of detonation was required to determine the time of flight of the ball bearing. Unfortunately, a foil trip-wire arrangement produced inconsistent detonation times, so the detonation time had to be inferred by some other means. This was achieved by identifying the specific characteristics of the detonation electromagnetic (EM) signal captured by the HPB. An example voltage-time history obtained from the experiments is shown in Figure 5. Although the exact peak voltages and spike timings vary, similar signals with particular identifying features (labelled t_1 to t_5 in Figure 6) were obtained for all experiments. To understand the signals and use them to identify the detonation time, an hypothesised detonation sequence is shown in Figure 6 for a generic electrical detonator (as the exact configuration of the M2A3 detonator used in this work is confidential). The basic components of generic electric detonators, namely a capacitor, a delay circuit made of resistors, a fuse head which explodes when the resistors are heated sufficiently and some primary explosives, are openly available [26].

A series of EM noises emitting from the detonation processes were expected in the following order. First, at time t_1, the capacitor would discharge through a typical exponential decay, to heat the bridge conductor [26]. Then the current flows into the delay circuit at the time t_2, which consists of a series of resistors. EM signals are expected as the current passed through them, causing the voltage spikes observed in Figure 5 and Figure 7. As specified delay detonators were not used herein, the exact duration of the delay is expected to vary as the manufacturer was not obligated to be consistent with the delay time. The temperature in the delay circuit increases until the fuse head explodes at t_3. This subsequently initiates the booster or a primary explosive [26] and thereafter, the detonation of the PE4. The explosion of the fuse head is thus the time of detonation for the detonator. The capacitor is physically further from the fuse than the circuit. This destruction is then accompanied by an additional EM pulse.

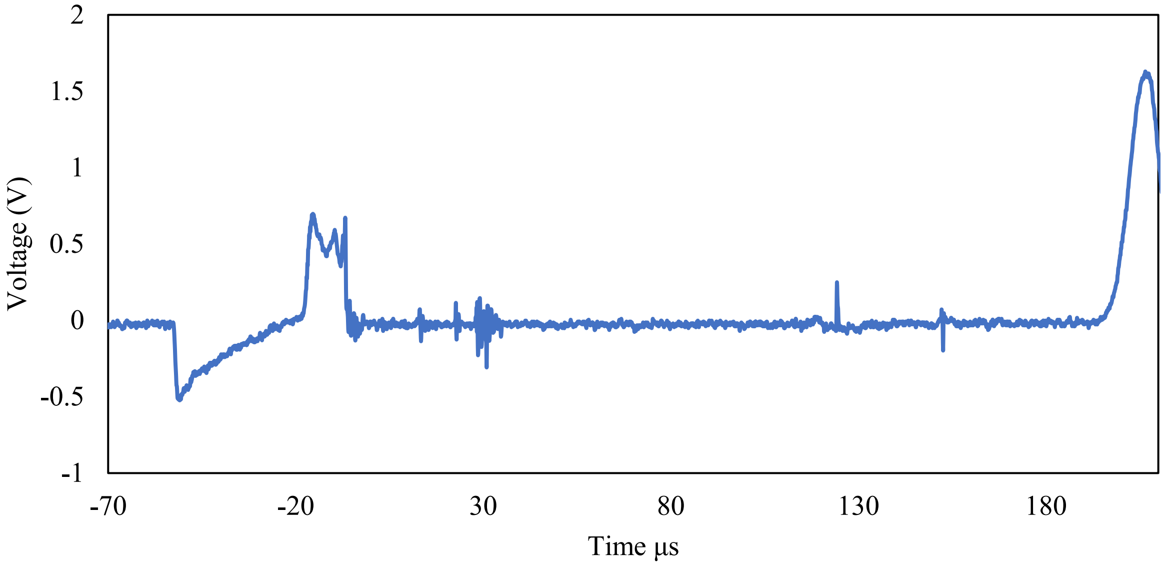

Figure 5 Typical example of a voltage-time history obtained during detonation (7.33 g PE4, 18 mm diameter charge).

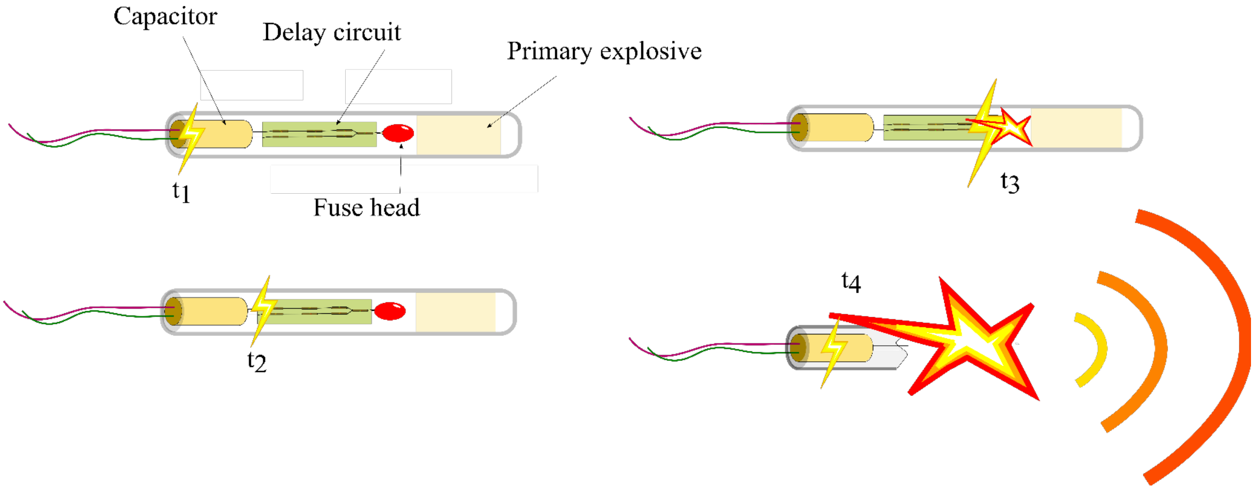

Figure 6: A schematic of a hypothesised detonation sequence from a typical electric detonator, composition of the detonator is adapted from ref [27].

A fictional model EM signal was generated using this hypothesis and is shown, for illustrative purposes only, in Figure 7, which is similar in form to Figure 5. Time, t_3, was treated as the signal of detonation and t_5 is the signal generated from the first shock wave on the HPB. The measurements using the above model allowed the detonation time (t_3) to be estimated and used to calculate the average velocity of the ball bearing, V_{avg}, using Eq. (2).

$$V_{avg} = \frac{\Delta x}{\Delta t} = \frac{\sqrt{x_{nor}+x_{dev}}+x_{gauge}}{t_{imp}-t_3-\frac{x_{gauge}}{C}+t_{detr}} \tag{2}$$

Where Δx is the total inflight distance of the ball bearing (a nominal distance of 100 mm), Δt is the inflight time, x_{nor} is the normal distance between the ball bearing and the witness plate, x_{dev} is the deviation from the centre of the witness bar to the centre of the impact crater, x_{gauge} is the distance from the front face of the HPB to the centre of the strain gauge, C is the speed of sound in the HPB and t_{detr} is the time it takes for the detonation wave to propagate the specific charge. t_{detr} was estimated using the ideal detonation velocity of PE4 at 8190 m/s [23].

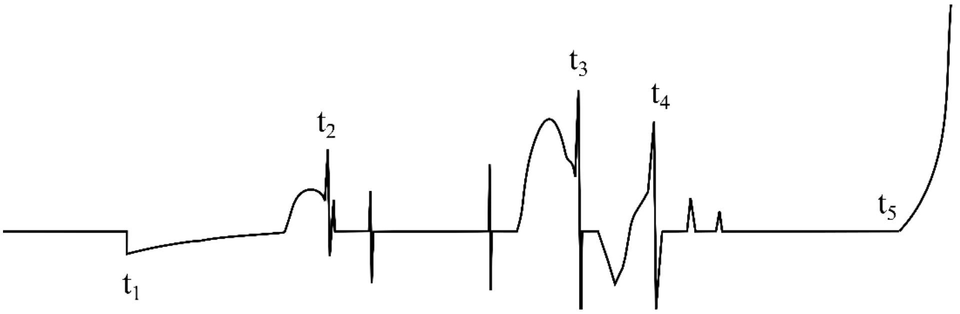

Figure 7: Illustrative (fictional) voltage trace developed from the hypothesised electrical detonation sequence.

3.4.2 Impact velocity of ball bearing

The impact velocity of the ball bearing on the aluminium witness plate was estimated using the crater depth. Prior to the blast tests, a series of impact experiments using a two-stage light inert gas gun were performed to develop an empirical relationship between impact crater depth and the ball bearing impact velocity. The standard gas gun arrangement was modified to accommodate a 5 mm ball bearing as the projectile, as detailed in reference [29-30]. Barrel exit velocities ranging from 200 to 580 m/s were used to correlate crater depth and impact velocity. A quadratic polynomial was fitted to the results, expressing velocity (v in m/s) in terms of crater depth (α in mm), shown in Equation 3. This was used to infer impact velocity using the measured crater depth during the blast experiments.

$$v(\alpha) = -4.833\alpha^2 + 164\alpha + 66.798 \tag{3}$$

4. Blast test results

In total, 21 blast tests were performed with the inclusion of a ball bearing. A summary of the measured data is presented in Table 2. For the ball bearing to impact the inner witness plate, the flight along the axis of symmetry must not deviate by more than 7°. More than 80% of the experiments achieved this level of axial alignment, allowing the HPB to measure useful information. The results are classified according to crater location, as shown in Figure 8, and defined as follows:

- A: the impact crater was circumscribed by diameter of the inner witness plate (seven tests)
- B: part of the crater was formed within the inner witness plate (ten tests)
- P: crater located on the outer witness plate (five tests)
- N: no crater found (one test)

Additionally, damage was caused to the tube wall and the significant fragmentation of ball bearing occurred during the 27g PE4 detonation shown in Figure 9 (f). Hence, no experiments were conducted above this charge mass.

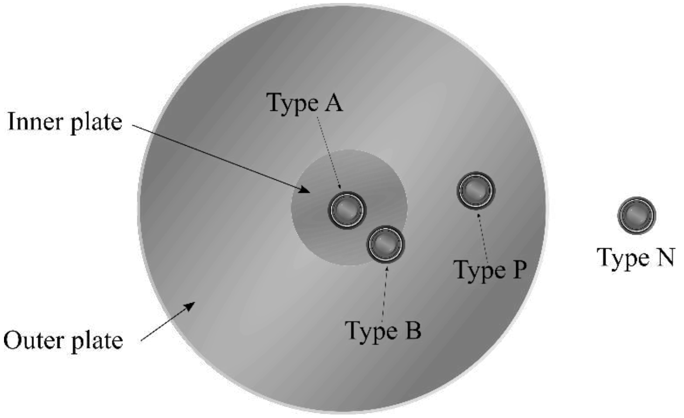

Figure 8: Classification of crater location types observed on the witness plates.

Table 2: Experimental results from the blast tests

Test ID	charge mass g	aspect ratio	Charge diameter mm	Charge Length mm	Result type	Crater depth mm	Crater offset* mm	Pendulum Impulse Ns	HPB Impulse Ns
2.20-0.3-18	2.2	0.3	18	5.4	B	1.54	10	5.5	0.47
3.67-0.5-18	3.67	0.5	18	9	A	2.24	3	7.3	0.63
4.40-0.6-18	4.4	0.6	18	10.8	P	2.11	22.5	7.8	N/A
5.13-0.7-18	5.13	0.7	18	12.6	B	2.26	10	8.7	0.71
5.87-0.8-18	5.87	0.8	18	14.4	B	3.18	9	9.4	0.77
7.33-1.0-18	7.33	1	18	18	B	3.47	12	10.9	0.82
8.07-1.1-18	8.07	1.1	18	19.8	N/A	N/A	N/A	10.9	N/A
9.53-1.3-18	9.51	1.3	18	23.4	B	3.75	9	10.7	0.91
11.00-1.5-18	11	1.5	18	27	P	2.5	16	14.0	0.8
5.21-03-24	5.21	0.3	24	7.2	A	1.9	4	9.8	0.62
6.953-04-24	6.95	0.4	24	9.6	B	2.745	8	11.3	0.78
10.43-06-24	10.42	0.6	24	14.4	A	2.94	3	16.6	1.36
13.91-08-24	13.91	0.8	24	19.2	A	3.55	7	19.2	2.17
17.38-1.0-24	17.38	1	24	24	N	N/A	N/A	24.7	1.50
6.79-02-30	6.79	0.2	30	6	P	1.68	19	13.7	0.69
13.58-04-30	13.58	0.4	30	12	B	2.8	10	22.3	2.19
20.37-06-30	20.37	0.6	30	18	B	3.955	10	26.4	N/A
27.16-0.8-30	27.16	0.8	30	24	A	N/A	7	36.4	3.46
5.87-0.1-36	5.87	0.1	36	3	P	1.12	15	12.5	0.65
11.73-0.2-36	11.73	0.2	36	6	B	2.13	10	22.00	2.38
17.60-0.3-36	17.38	0.3	36	9	B	3.31	11	32.2	1.60
9.32-01-42	9.32	0.1	42	4.2	A	1.36	6	19.2	2.21
18.63-02-42	18.63	0.2	42	8.4	A	2.28	7	34.1	2.56

**Crater offset is the centre-to-centre distance between the witness plate centre and the crater.*

4.1 Witness plate damage

Photographs of the selected witness plates are presented in Figure 9, arranged according to increasing explosive charge mass. Some small dimples were observed across the face of the witness plates in addition to the ball bearing crater, as shown in Figures 9(d). An additional test was performed to determine if the small dimples could be a detonator effect. A single detonator (no additional charge or ball bearing) was detonated at the open end of the blast tube. The effect on the witness plate is shown in Figure 9(a). Small dimples were evenly distributed across the witness plate surface, caused by micro-impacts from the detonator casing. Thus, damage from the detonator probably caused the dimples shown in Figure 9(d), which are scattered across the witness plate, while the damage localised to the crater in Figure 9(b, c) may be due to the ball bearing itself. There was a reduction in the small dimpling effect from the detonator as the charge mass increased, as might be expected.

It was also noted during the experiment with only the detonator that the impulse from the detonator is extremely limited as it could not even trigger the recording of the pendulum movement.

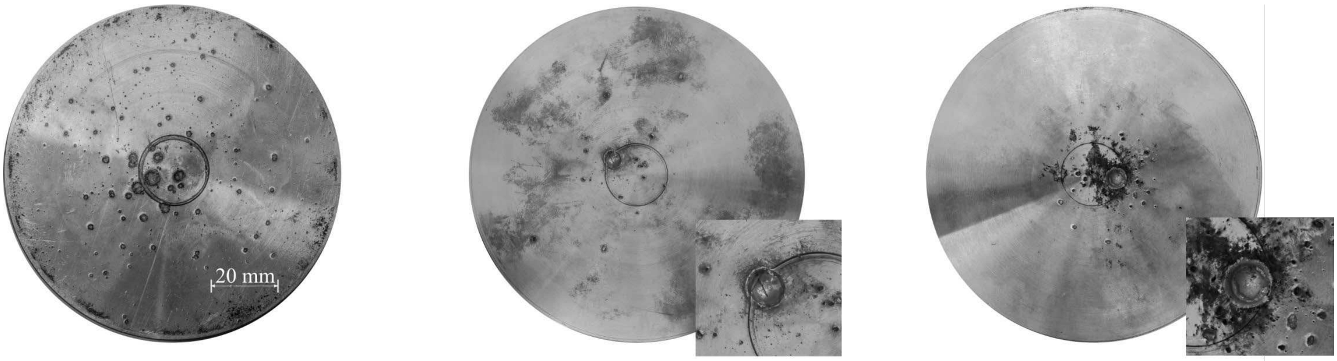

a) Detonator only b) 2.20-18-0.3 c) 5.87-18-0.8

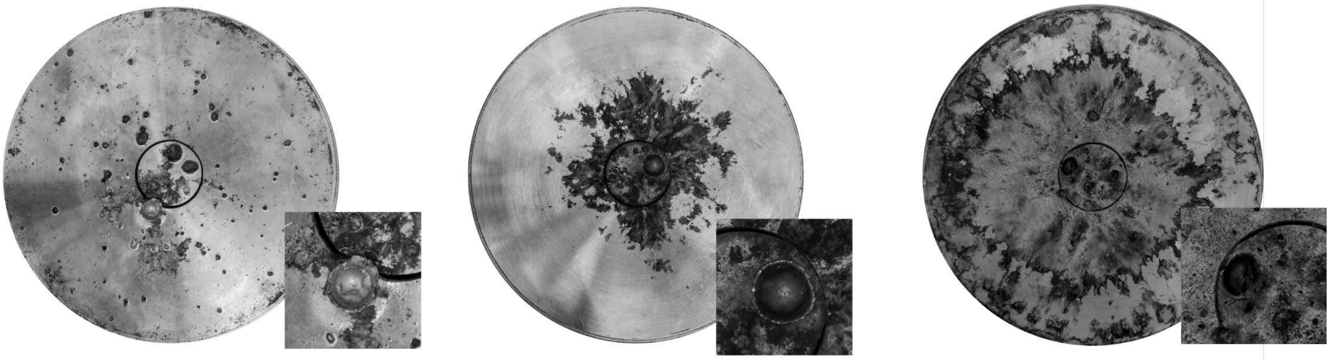

d) 7.33-18-1.0 e) 13.91-24-0.8 f) 27.16-30-0.6

Figure 9: Photographs of typical witness plates from the experiments, (arranged according to the charge mass). The crater caused by the ball bearing impact has been enlarged for clarity.

For detonations above 10 g PE4, the witness plates generally exhibited a single crater from the ball bearing and some discolouration as shown in Figures 9(e) and 9(f). The discolouration was not evident in smaller explosive mass tests, and resembled burn marks on the aluminium alloy surface, probably due to the fireball. Assuming a TNT equivalency value of 1.2 for PE4, the Hopkinson scaled distance (*Z*) values for the detonations above 10g are below 0.44 m/kg$^{1/3}$. It is known that the (initially very hot) fireball continues to expand until it reaches Z of 1 m/kg$^{1/3}$ [31], so it is plausible the fireball is at sufficiently high temperature to mark the surface of the aluminium alloy witness plate for 0.31 m/kg$^{1/3}$ $< Z <$ 0.44 m/kg$^{1/3}$.

4.2 Ball bearing damage

Twelve (57 %) of the blasted ball bearings were recovered post-test. Photographs of typical specimens are shown in Figure 10, where m_0 and m_a are the pre- and post-test ball bearing masses respectively. The maximum mass loss was 6.8 % and the arithmetic mean mass loss was 2.8 % (using the mean mass of the ball bearing measured prior to blasting). In most cases, it was not possible to recover the bearings immediately after each experiment, so only two of the recovered ball bearings are linked to a particular experiment (Figure 10a and 10b). However, general features of the post-test ball bearings are described herein. From Figure 10, it is evident that the post-test ball bearings were no longer spherical and sustained significant damage. One-half of the bearing had darkened in colour, while the other half had a shiny appearance and appeared significantly flattened. This will be discussed further in conjunction with the computational simulation results.

a) 4.40-18-0.6
$m_0 = 0.50445$ g
$m_a = 0.50452$ g

b) 5.13-18-0.7
$m_0 = 0.505344$ g
$m_a = 0.47420$ g

c)
$m_a = 0.48660$ g

d)
$m_a = 0.50309$

Figure 10: Photographs of typical post-test ball bearings

4.3 Impulse results

A graph of axial impulse inferred from the pendulum swing versus charge mass is presented in Figure 11, grouped by the charge diameter. At a constant charge diameter, pendulum impulse increased linearly with the increase in charge mass, as expected. Figure 11 shows that the pendulum impulse was consistent, irrespective of the ball bearing crater location (A, B, or P). The pendulum impulse also increased with charge diameter, which was also expected. A graph of HPB impulse versus pendulum impulse is shown in Figure 12. Since the HPB covered 4 % of the total area of the witness plate, it would be expected that a uniformly distributed blast loading would transfer 4 % of the pendulum impulse to the HPB (indicated by the solid line in Figure 12). However, the impulse captured by the bar was more than twice that anticipated for a uniformly distributed load. This suggests that the blast pressure experienced at the witness plate is non-uniform which agrees with the observation made by Cloete and Nurick [25] for this blast tube length.

Figure 12 shows that in general, the HPB impulse increased linearly with increasing pendulum impulse. As it the distribution of the impulse was shown to be localised in the centre, it was unsurprisingly to observed that HPB impulse was more sensitive to the crater location. HPB impulse for result types A and B were both observed to be at 9% of the pendulum impulse using a linear fit with correlation coefficient above 0.97. Impulse from result P yielded smaller HPB impulse (6% of pendulum impulse). The 3% difference cannot to attributed to the absence of impact on the HPB in result type P since the effect of the ball bearing had already been removed in the HPB impulse calculation using Equation 1. Due to the sensitivity of the HPB impulse on the correct alignment of the experiment, result type P was not used in the rest of the impulse analysis.

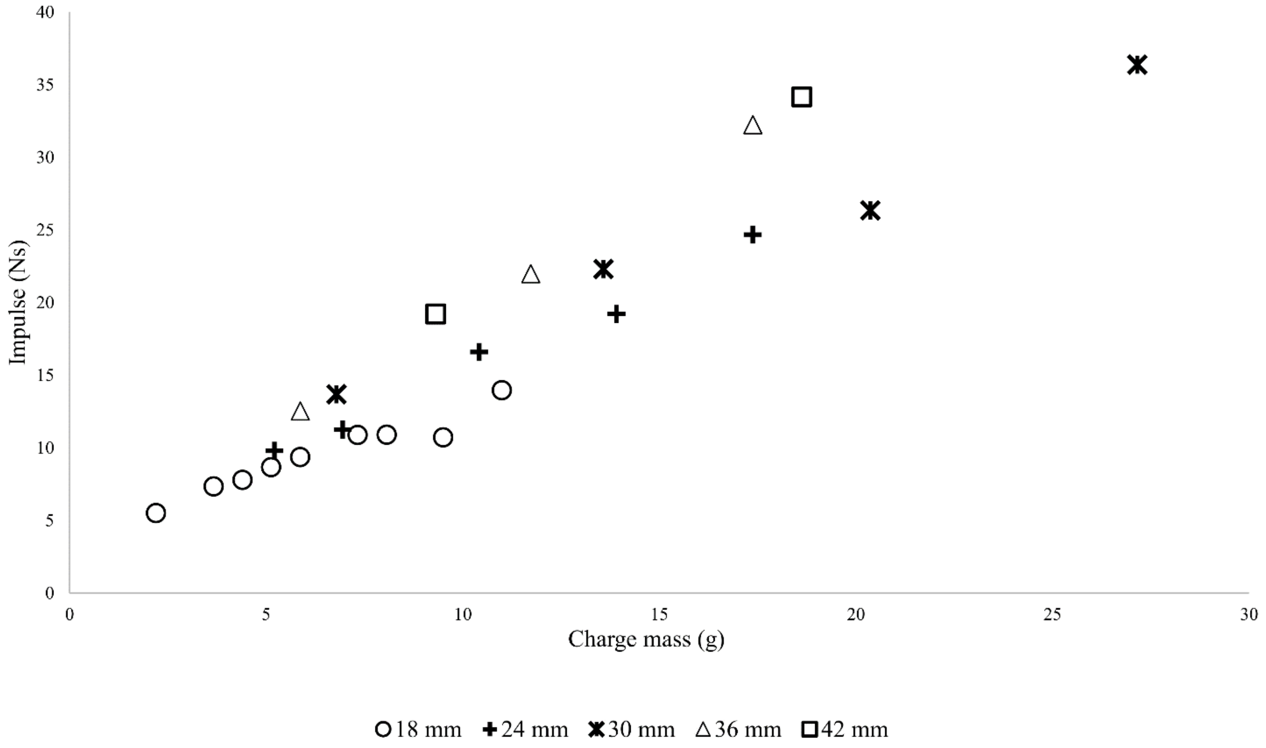

Figure 11: Graph of axial impulse versus charge mass, grouped by charge diameter

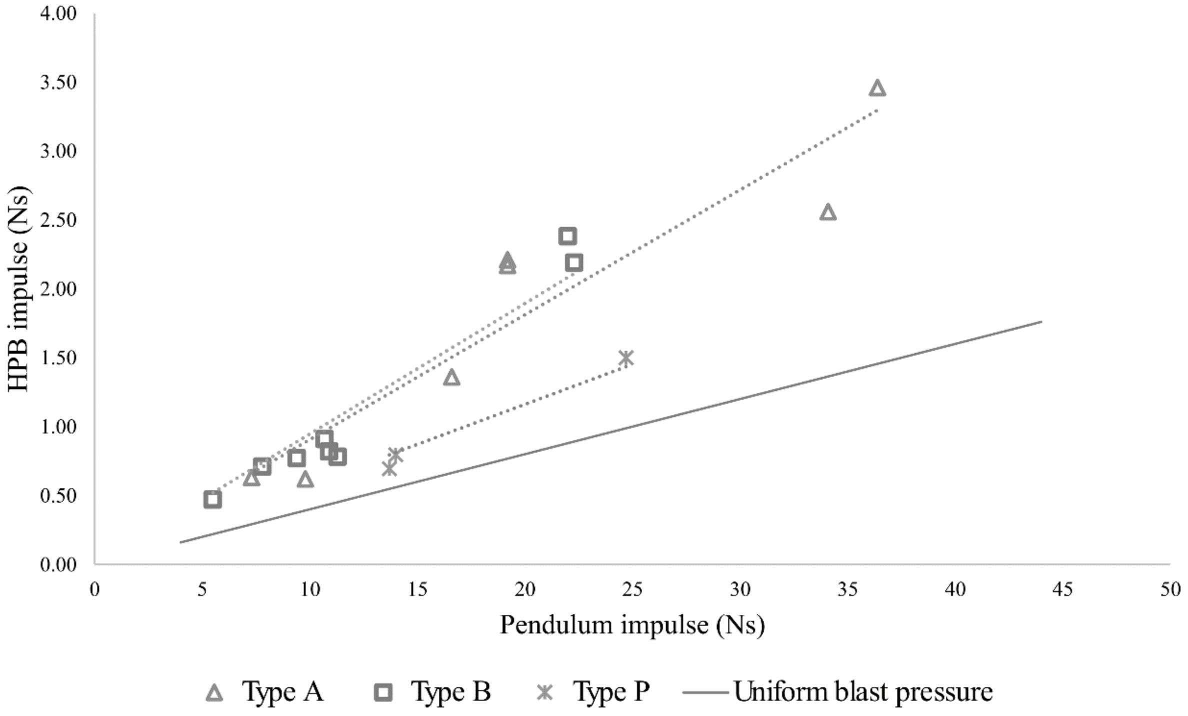

Figure 12: Graph of HPB impulse versus pendulum impulse

4.4 Ball bearing velocity results

The impact and average ball bearing velocity results are shown in Table 3. It should be noted that the application of Equation 3 to impact velocity calculations from the blast experiments results in velocities that exceeded the range of the gas gun experiments in some cases. The highest impact velocity in Table 3 is 640 m/s, which is 10.3% higher than the maximum bearing velocity obtained in the gas gun experiments. While it is unfortunately not possible to increase the velocity of the gas gun ball bearing tests, the high thickness of the witness plate makes an approximately 10% extrapolation a reasonable assumption.

In general, the average velocities are higher than the impact velocities, suggesting that the ball bearing may have been slowed down by the reflected blast pressure waves prior to impact. A graph of average velocity versus charge mass is shown in Figure 13.The average velocity results seem to overlap for these two charge diameters at low charge masses, but at higher charge masses the 18 mm diameter charges produced higher average velocities.

The impact velocity results are shown in Figure 14. The impact velocities seem to group into two bands – one for the Ø18 mm and Ø 24 mm charges, and one for the Ø30, Ø36, and Ø42 mm charges. Similar to the average velocity results, the impact velocity decreased with the increase in charge diameter for Ø18 mm and Ø 24 mm charges when the charge mass increased above 7 g. The impact velocities for the Ø30 to Ø42 mm charges are all much lower, but within the Ø30 to Ø42 mm charge group it is difficult to observe any influence, possibly due to the small number of tests. For all charge diameters, a non-linear increase was observed with the increase in charge mass, which is proportional to an increase to charge aspect ratio at constant diameters.

Table 3: Impact and average velocities from the physical blast tests

Test ID	Impact Velocity	Average velocity
2.20-0.3-18	308	371.4
3.67-0.5-18	410	478.6
4.40-0.6-18	392	N/A
5.13-0.7-18	413	492.9
5.87-0.8-18	540	529.2
7.33-1.0-18	578	473.2
9.53-1.3-18	614	643.6
11.00-1.5-18	447	N/A
5.21-03-24	361	414.9
6.953-04-24	481	492.1
10.43-06-24	508	606.1
13.91-08-24	589	643.0
6.79-02-30	329	N/A
13.58-04-30	488	576.4
20.37-06-30	640	N/A
5.87-0.1-36	245	N/A
11.73-0.2-36	394	434.8
17.60-0.3-36	557	N/A
9.32-01-42	281	307.0
18.63-02-42	416	431.5

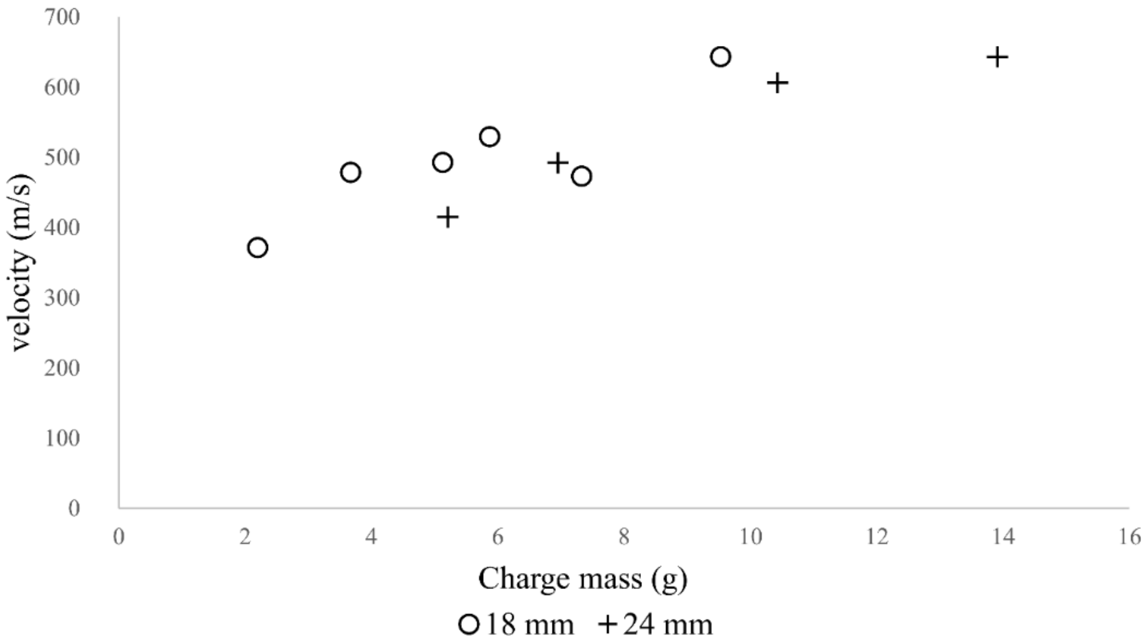

Figure 13: Graph of the average velocity versus charge mass for the Ø 18 and Ø 24 mm charges

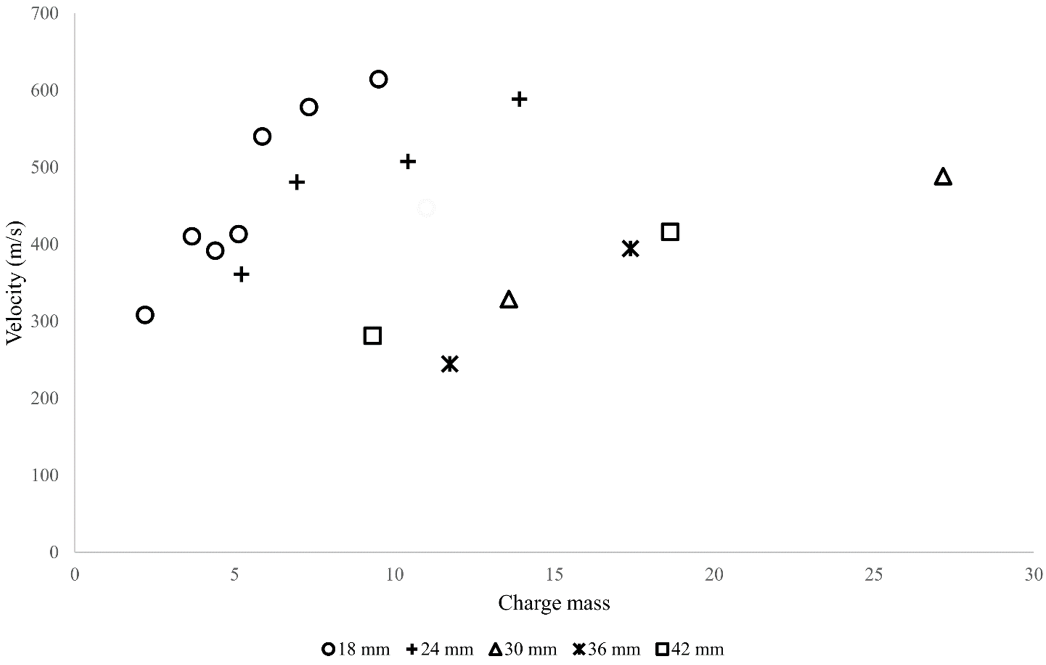

Figure 14: Graph of impact velocity versus charge mass, grouped by charge diameters

5. Computational model development

Computational simulations were performed using the commercial hydrocode ANSYS Autodyn version 18. A two-dimensional axisymmetric model was constructed using the geometries from the experimental arrangement, as shown in Figure 15.

5.1 Geometry and boundary conditions

The front clamp, back clamp and HPB were modelled as fixed boundaries that were applied on the witness plates. In the experimental arrangement, a 10 mm steel backing plate was placed behind the outer witness plate. The inner witness plate was backed by the HPB. For the duration of the experiment, the witness plate assembly was assumed to not have translated in the x direction, hence the boundary condition was applied to simulate the influence of the steel plate and the HPB.

The blast tube wall was modelled as a reflective boundary. An 'outflow' boundary condition was applied to simulate the blast chamber environment where the charge was detonated. The rest of the pendulum, along with the EPS bridge, and aluminium foil were not included in the simulation. The dimensions of the Euler air mesh were 162 mm by 51.15 mm. Following a mesh sensitivity study (details can be found in ref [30]), a 0.2 mm mesh side length was chosen for the air and explosive parts. This allowed for a minimum of 45 elements (for the 18 mm diameter charge) across the explosive radius, with the number of elements increasing with increased charge diameter. This is far finer than the ten element minimum rule-of-thumb recommended by Schwer and Rigby [32] to adequately represent the explosive energy release. The witness plates were modelled using two rectangular parts. The rear faces of witness plates were fixed in the x-direction. A 3.2 mm line detonation was used to simulate the Ø 6.4 mm detonator used in the blast tests. The detonation initiated simultaneously across its line in the simulation.

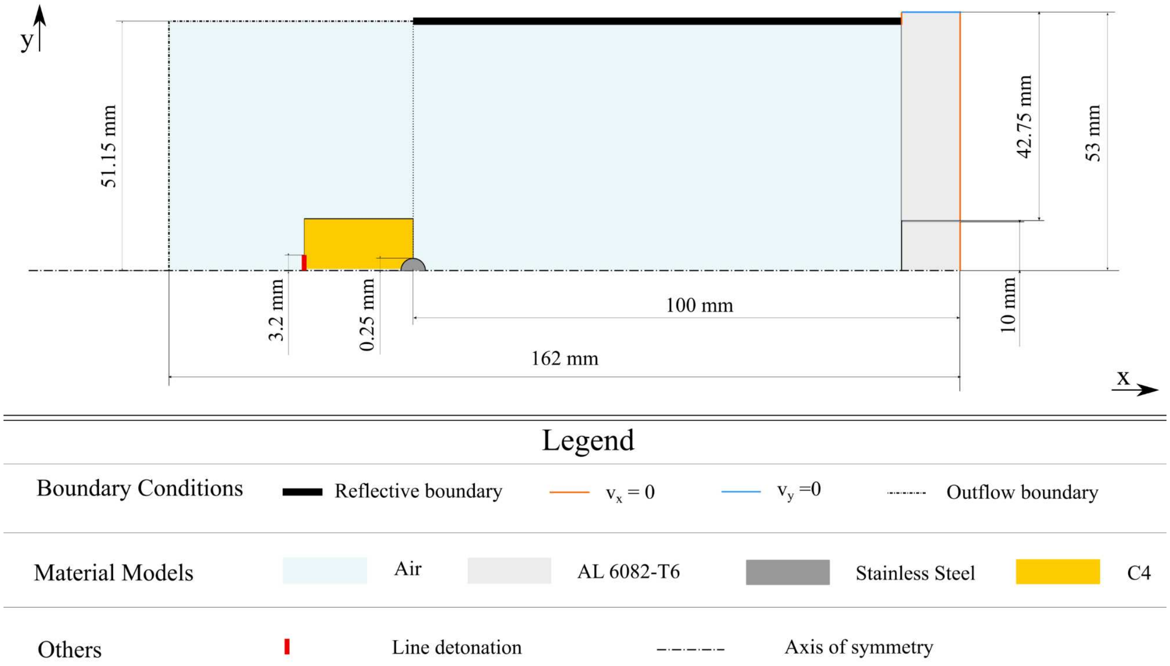

Figure 15: Schematic showing the geometry and boundary conditions used in the Autodyn simulations

5.2 Material formulation

The ideal gas model was used for the air mesh. Numerical pressure gauges were placed at 0.4 mm intervals across the rear face of the blast tube. Summation of blast pressure over time using the trapezoidal rule was used to calculate the pendulum and HPB impulse over the appropriate areas. Similar to previous works [23, 33], the JWL parameters for C4 were used to model PE4 [34]. C4 and PE4 contain similar proportions of the active explosive RDX (C4 contains 91%, PE4 has 88%) and differ in terms of binders used [35], so the explosive parameters for C4 are commonly used in the modelling of PE4 detonations [32]. Bogosian et al [35] studied the equivalence of C4 and PE4 and concluded, for impulse and pressure equivalence, the two explosives can be treated as the same material. Details of the air and C4 model parameters are in Table 4.

The Johnson-Cook strength model [36] was selected for the Al6082-T6 witness plates using the parameters proposed by Yibo et al [37]. A model of the tensile tests was used to check that the parameters found by Yibo et al [37] would reproduce the physical test results report in Table 1. At the $0.001s^{-1}$ strain rate, the 0.2% proof strength and ultimate tensile strength from the model were within 2.4 % and 3.2 %, respectively, of the physical test results. The STNL.STEEL model available in the Autodyn material library [38] was used model stainless steel AISI 420C. Although the ball bearings were not characterised, simulation results showed that the strength properties of the ball bearing (including the deformation exhibited during initial blasting), had little effect on the velocity characteristics in-flight. Properties used for STNL.STEEL and Al 6082-T6 are shown in Table 5.

Table 4: Properties of Air and C4 used in the simulation

Air (Ideal gas)			C4 (JWL)			
Density (g/cm^3)	Gamma	Specific Heat (J/kgK)	Density (g/cm^3)	A (GPa)	B (GPa)	R1
			1.601	610	13	4.5
0.001225	1.4	717.6	R2	W	C-J velocity (m/s)	C-J Pressure (GPa)
			1.4	0.25	8190	28

Table 5: Properties of Al6082-T6 and STNL.STEEL used in the Autodyn simulations

Al 6082-T6 (Johnson-Cook, from [36])			STNL.STEEL (Piecewise Johnson-Cook, from [38])		
Shear Modulus (GPa)	Yield strength (MPa)	Hardening constant (MPa)	Shear Modulus (GPa)	Yield Stress (MPa)	Eff. Plastic Strain # 1
27.6	306	304.9	73	689	0.3
Hardening Exponent	Strain Rate Constant	Thermal Softening Exponent	Yield Strength #1 (GPa)	Strain Rate Constant	Thermal Softening Exponent
0.68	4.37×10 −3	1	1	4.37×10 −3	1

5.3 Simulation results

A total of 48 axisymmetric simulations were performed using ANSYS Autodyn v.18.0. The results are summarised in Table 6. The computational simulations covered a greater range of charge masses and aspect ratios than the physical experiments. The results that overlap with the experiments were used to validate the modelling predictions, while the extra simulations elucidated the effects of charge mass and geometry on the ball bearing flight velocity.

Table 6: Simulated impulse and velocity results

Charge mass	Charge Diameter	Aspect Ratio	Total impulse	Bar impulse	Impact velocity	Average Velocity	Peak Velocity
2.20	18	0.3	5.6	0.39	310	321	328
2.93	18	0.4	7.0	0.48	376	394	410
3.67	18	0.5	8.2	0.58	432	470	470
4.40	18	0.6	9.3	0.66	476	495	515
5.13	18	0.7	10.0	0.71	499	520	540
5.87	18	0.8	11.1	0.79	537	561	580
6.60	18	0.9	10.6	0.77	553	575	604
7.33	18	1	11.0	0.79	561	590	623
8.07	18	1.1	12.6	0.85	572	598	638
9.53	18	1.3	13.4	0.90	600	625	662
11.00	18	1.5	13.8	0.92	606	630	678
14.67	18	2	14.5	0.94	637	656	703
5.21	24	0.3	12.1	0.66	384	402	425

6.95	24	0.4	15.2	0.83	459	483	515
8.69	24	0.5	17.8	0.97	510	540	582
10.43	24	0.6	20.0	1.07	554	595	634
12.17	24	0.7	21.6	1.15	593	625	676
13.91	24	0.8	22.0	1.20	624	655	710
15.64	24	0.9	24.0	1.30	646	684	737
17.38	24	1	25.0	1.35	659	699	760
19.12	24	1.1	25.7	1.39	680	721	780
22.60	24	1.3	26.8	1.45	700	743	812
26.07	24	1.5	27.5	1.51	713	748	834
34.77	24	2	28.5	1.59	734	773	868
6.79	30	0.2	16.0	0.83	333	351	373
10.19	30	0.3	22.3	1.16	435	466	508
13.58	30	0.4	27.0	1.45	501	544	606
16.98	30	0.5	31.1	1.69	554	606	681
20.37	30	0.6	35.4	1.92	593	654	740
23.77	30	0.7	38.3	2.05	621	687	788
27.16	30	0.8	39.1	2.11	646	720	826
33.95	30	1	38.6	2.22	688	767	887
44.14	30	1.3	45.1	2.66	728	805	947
11.73	36	0.2	26.6	1.37	373	398	436
17.60	36	0.3	35.6	1.85	486	526	581
23.47	36	0.4	41.2	2.24	547	610	688
29.33	36	0.5	49.5	2.71	587	663	771
35.20	36	0.6	55.6	3.05	621	708	837
41.07	36	0.7	60.1	3.35	645	741	890
46.93	36	0.8	64.9	3.61	661	772	934
9.32	42	0.1	22.2	1.16	228	241	261
18.63	42	0.2	39.8	2.01	414	444	493
27.95	42	0.3	52.2	2.86	511	564	653
37.26	42	0.4	67.2	3.53	558	643	764
46.58	42	0.5	74.9	4.06	574	687	855
55.90	42	0.6	85.8	4.65	587	729	932
65.21	42	0.7	93.2	5.02	604	767	985
74.53	42	0.8	98.4	5.31	619	791	1033

6. Discussion

6.1 Axial impulse

The impulses obtained from simulations (normalised according to the experimental impulses) are shown in Figure 16. The closed symbols represent the HPB impulses while the open symbols are the pendulum impulses. The simulations tend to over-estimate the pendulum impulses and under-predict the HPB impulses. The mean pendulum impulse over-estimation was +15.7%. The computational simulations assumed that all the gas pressure at the rear face of the blast tube was converted to axial impulse, and the inner wall of the blast tube was modelled as a reflective boundary. In the physical experiment, impulse transfer may be reduced if these assumptions were not completely realistic (for example, some of the blast waves may exit the blast tube and not contribute to the impulse, and the walls of the blast tube will not be frictionless and rigid). The normalised simulated HPB impulses are consistently less than 1, meaning that the simulations under-predict the HPB impulse (by -30% on average). There is more scatter in the HPB data, reflecting the higher amounts of scatter in the experiments. The two normalised impulse ratios appear to be independent of charge mass and diameter which means that the trends in the simulated impulse values matches the experimental ones for the same charge mass range, although the magnitudes are different.

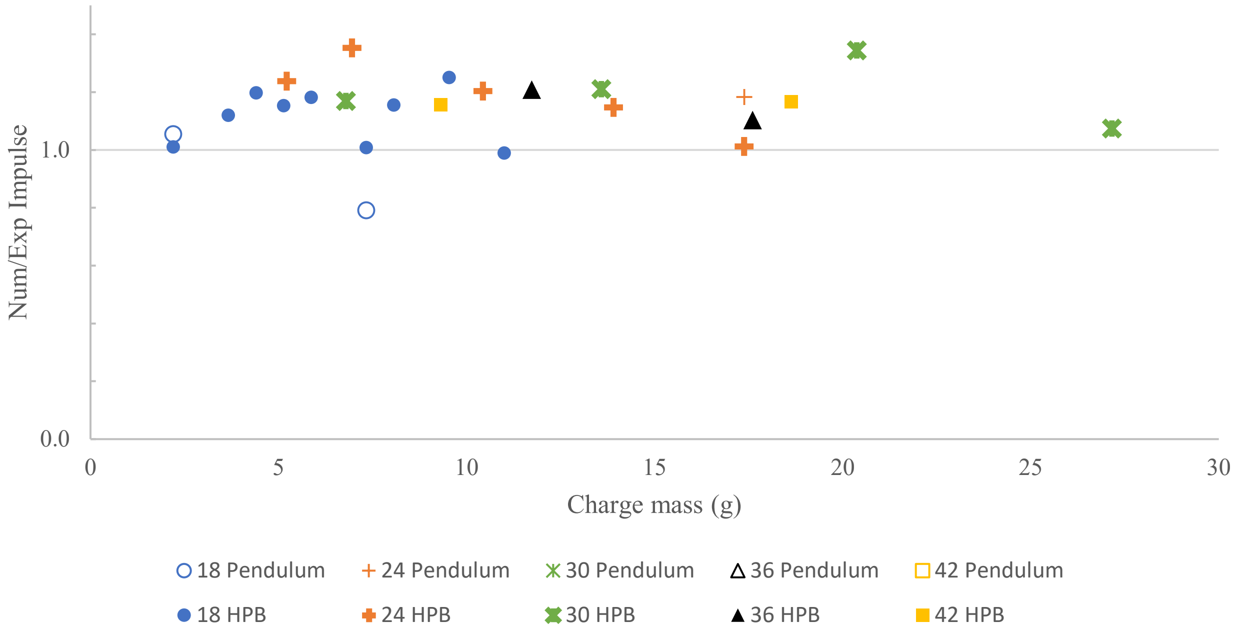

Figure 16: Graph of simulated impulse values normalised against experimental results versus charge mass

Computational simulations were performed to extend the range of the physical experiments, which were limited in charge mass by the deformation of the blast tube for PE4 detonations above 25 g. A graph of simulated pendulum impulse versus charge mass is shown in Figure 17, extending the simulations beyond the physical test range. The results are grouped by charge diameter. The initial parts of the curves are similar to the physical experiments, but as the charge mass increased, the rate of pendulum impulse decreased, leading to a plateau in impulse (beyond which, an increase in charge mass did not cause an increase in impulse). This has been previously attributed to the increasing lateral blast wave component and the interference between the radial and axial blast waves [6-9].

Kennedy [13] simplified this complexity using the concept of an effective charge mass, and estimated maximum effective charge heights for a given cylindrical charge diameter, i.e. critical charge aspect of $\sqrt{3}/2$. As expected, the charge mass (and therefore charge height) at which this plateau in the axial impulse occurred increased with increasing charge diameter. The difference in axial impulse imparted by same mass cylindrical charges with different diameters is more visible at higher charge masses. A 4th order polynomial function was fitted through the simulation data to show the non-linear impulse-charge mass relationship which was not as apparent in the experiments because of the limited charge mass range.

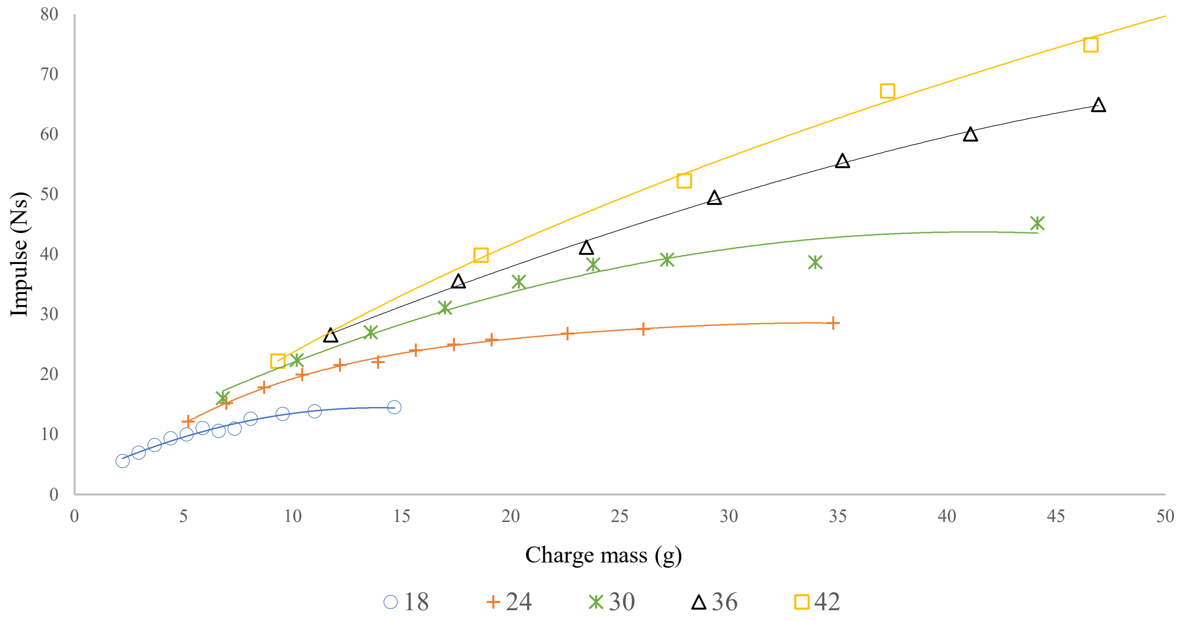

Figure 17: Graph of the simulated pendulum impulse versus charge mass, grouped by charge diameter

The graph of HPB impulse versus total axial impulse obtained experimentally and numerically is shown in Figure 18. A strong linear correlation (R^2 correlation coefficient = 0.996) was observed for the numerical results. As expected, the 0.888 correlation coefficient for the experimental results was slightly lower, due to experimental scatter, but still indicated a strong positive correlation. The experimental HPB impulse results indicated that the load distribution was localised in the centre (on the HPB face). This is illustrated in Figure 18, where the magnitudes of the experimental HPB impulses are much higher than the dotted line that represents the impulse that would be imparted to the HPB (4 % of the pendulum value) based on a uniform load assumption.

The simulated HPB impulse values, shown by the blue circles, are also greater than the uniform load distribution would calculate, albeit less than the experimentally obtained values. Both the computational and experimental results show localisation of the loading to the central location, with the HPB impulses being 9.45% (experimentally) or 5.28% of the pendulum impulse, despite representing 4% of the area. The computational simulations do not predict as much load localisation as observed experimentally. This difference may be evidence of local irregularities not captured in the model physics. Rigby et al [4] observed variations in the loading resulting from *L/D* = 1/3 cylindrical charge detonations, and hypothesised that these were due to local irregularities due to Rayleigh-Taylor [39-40] and Richtmyer-Meshkov [41-42] instabilities on the surface of the expanding detonation product cloud. Rigby et al [4] suggested that distance between the charge and the target, nominally $Z = 0.37$ m/kg$^{1/3}$, made these instabilities more prominent and caused considerable variations in the spatial distribution of pressure and impulse across the target face. In the current experiments, the aspect ratios overlap with ref [4] and Hopkinson-Cranz scaled distances are comparable for detonations above 10 g

(0.31 m/kg$^{1/3}$ < Z < 0.44 m/kg$^{1/3}$). Surface instabilities are hypothesised to be present in the physical detonation product cloud which would not be captured in the computational simulations. Thus, the additional rise in impulse observed experimentally is attributed to instabilities that cause localised peaks in pressure on the HPB face in addition to localisation of the pressure loading.

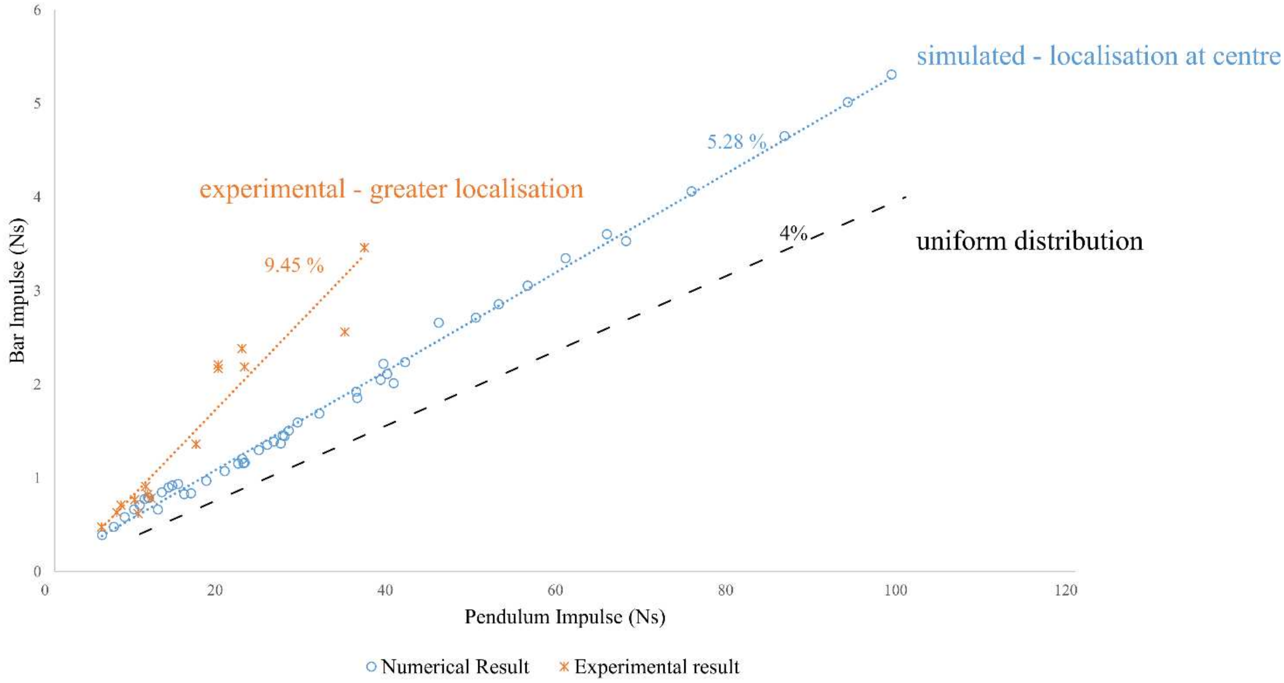

Figure 18: Graph of HPB impulse versus the pendulum impulse

6.2 Blast arrival time

Experimentally, the blast arrival time was estimated using the difference ($t_5 - t_3$). This is plotted against charge length in the graph in Figure 19 and compared to the blast arrival times determined from computational simulations. The experimental data is scattered around the best fit line fitted through the simulation data, for the full range of physical tests. The computational simulations exhibited none of the scatter present in the experiments, indicating that the blast arrival times from the experiments should be treated with caution. The mean arrival time using the experimental estimates was 16.8 μs, compared to the simulated mean arrival time mean of 19.0 μs. The largest deviation in blast arrival time between the simulations and experiments was 11.8 μs. However, when considered in the context of the ball bearing time of flight (174.4 μs for the experiment with the largest time difference), an 11.8 μs variation is approximately 6.7 % of the flight time.

Some trends were observed from the simulation results shown in Figure 19. Firstly, all the data seemed to fit one line of best fit, with only small deviations caused by the differences in charge diameter. There was a minimum blast arrival time of 18 μs when the charge length was 14 mm. Arrival times for charge lengths below 14 mm (identified as zone 1) were more sensitive to changes in length than those above 14 mm (zone 2). The differences in arrival time for a given charge length were almost insensitive to charge diameter (and therefore independent of charge mass). This behaviour is attributed to the development of the detonation pressure within the explosive charge and is discussed later.

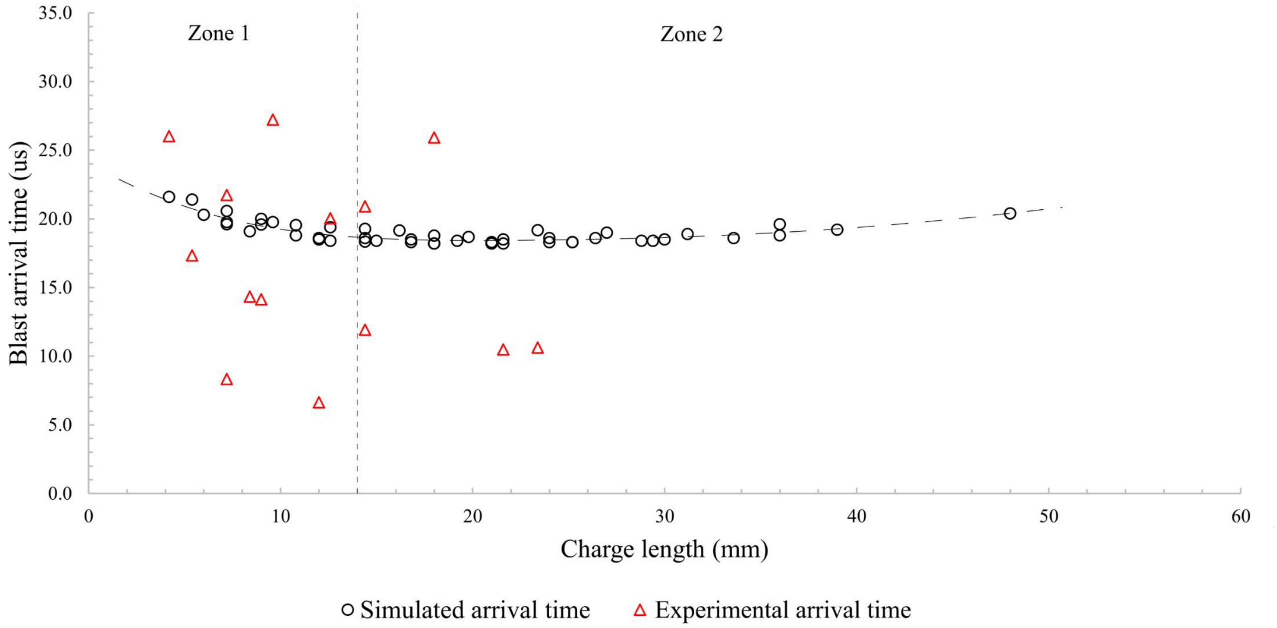

Figure 19: Graph of blast arrival time versus charge length

6.3 Impact and average ball bearing velocity

The normalised (with the corresponding experimental value) simulated impact and average ball bearing velocities are shown in Figure 20, plotted against charge mass. No distinct influences of charge mass, diameter, velocity (impact or average) is evident. The mean variation in the simulated impact and average velocity were +1.1% and +1.8 % with standard deviations of 12% and 13%, respectively. Therefore, the results shown in Figure 20 provide confidence in validation of the ball bearing velocity simulations.

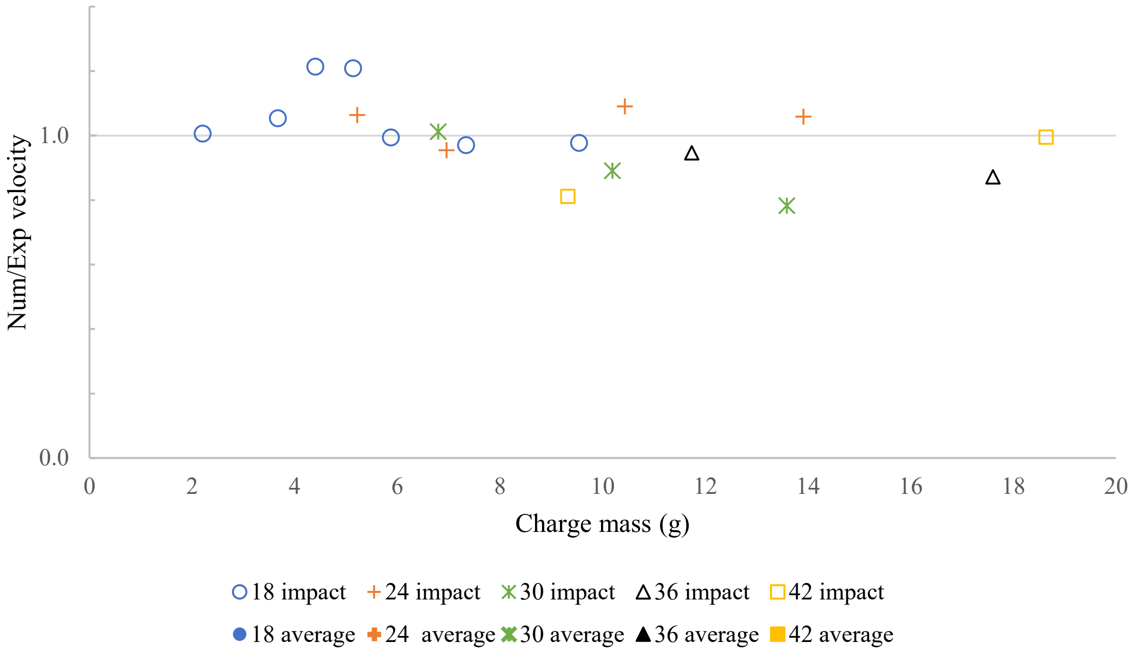

Figure 20: Graph of the ratio of numerical and experimental impact and average velocity

6.4 Ball bearing flight velocity simulations

Typical flight characteristics

The simulation results were used to provide additional insight into the ball bearing flight that could not be measured experimentally. A typical ball bearing velocity and acceleration history is shown in Figure 21 (a) from the detonation time to the arrival of the ball bearing at the witness plate. The impact history is shown in Figure 21 (b) where the ball bearing's velocity decreased nearly linearly and remained constant after the rebound. The large spikes in the acceleration are partly due to numerical errors generated from limited temporal resolution in the model. However, since impact simulation is not the focus of the paper and is complex in nature, additional analysis is presented in ref [43].

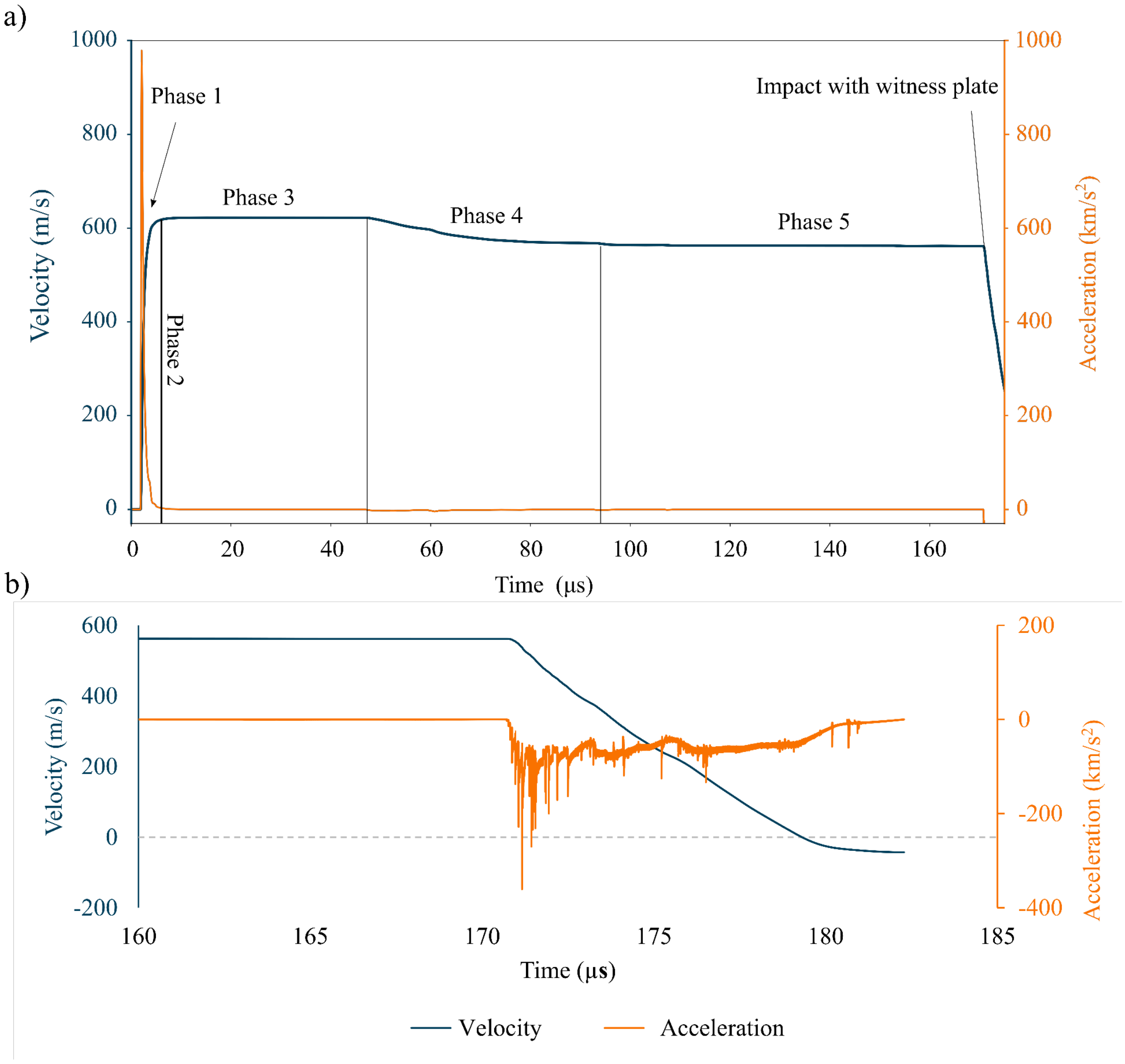

Figure 21: Graph showing the simulated acceleration and velocity histories for a Ø 18 mm, *L/D*=1 detonation, a) the during the ball bearing flight, b) during the impact with the witness plate.

The ball bearing flight was divided into five phases based on the driving mechanisms within each zone. Figure 22 contains pressure contour plots, velocity-time and acceleration-time histories at four times, from four of the identified phases of flight.

The first phase is from detonation initiation to completion, where the ball bearing begins to acquire momentum. A typical pressure contour 2.532 μs after detonation is shown in Figure 22 (a). At this point, the detonation within the charge had completed and the acceleration profile showed a high spike in the acceleration of the ball bearing. The maximum pressure at the shock front was considerably lower than the C-J pressure. The ball bearing velocity rapidly increased since its acceleration was still positive in the axial direction throughout this phase. The detonation products and the shock front were still behind the ball bearing.

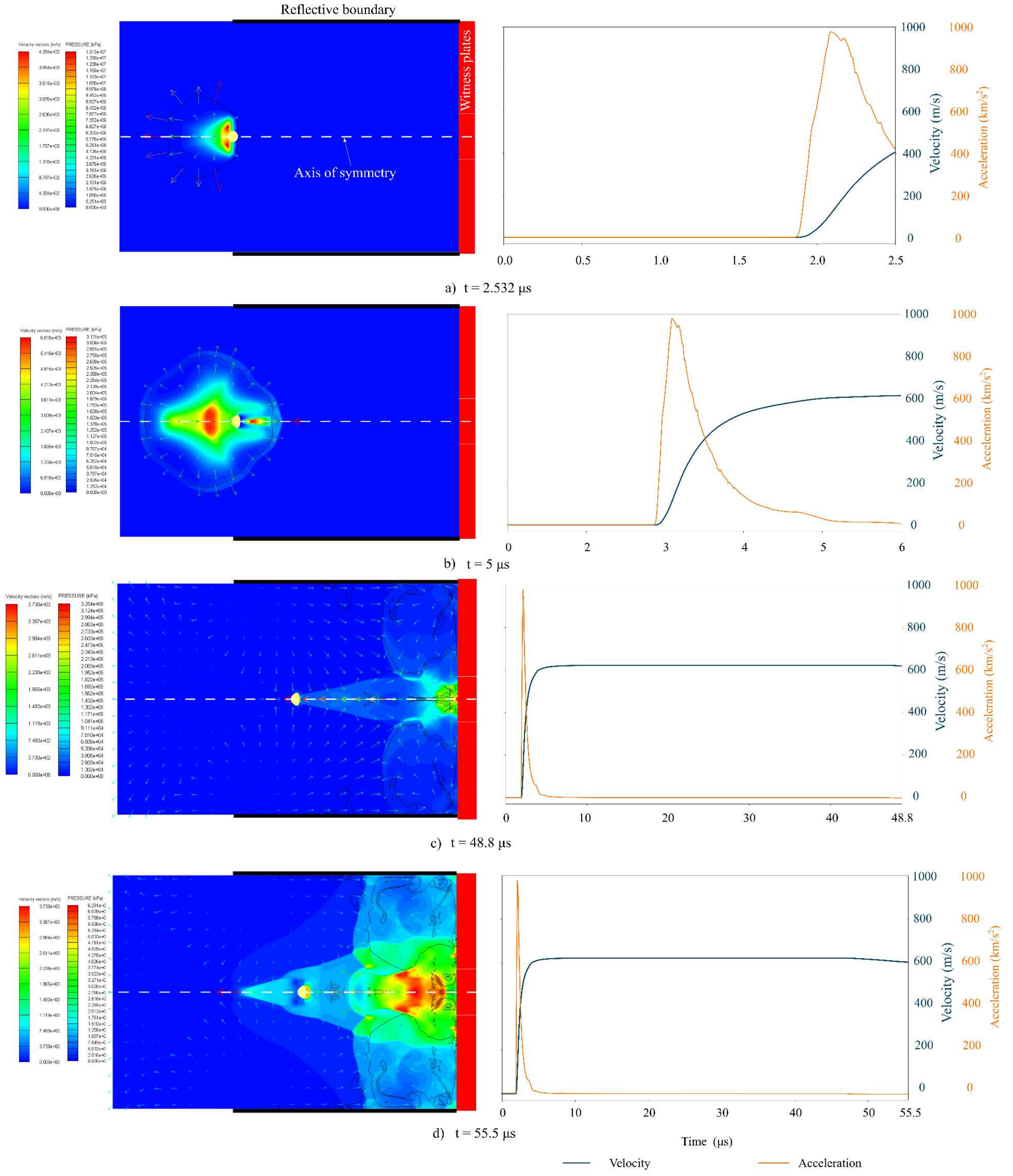

a) t = 2.532 µs

b) t = 5 µs

c) t = 48.8 µs

d) t = 55.5 µs

Figure 22: Simulated pressure contours, velocity vectors (left), velocity and acceleration histories (right) at different times experienced by a typical ball bearing for a Ø 18 mm, *L/D*=1 detonation.

In the second phase, the shock front overtook the ball bearing and the maximum pressure in the expanding gas cloud decreased significantly. A representative point in time, t = 5 μs, is shown in Figure 22 (b). The acceleration of the ball bearing decreased sharply and the ball bearing velocity began to plateau. In the third phase, shown in Figure 22(c), the ball bearing maintained its constant (maximum) velocity as there was insignificant pressure difference across the ball bearing during its flight through the rarefaction expansion waves. After t = 48.8 μs, reflected blast waves began to interact with the ball bearing, initiating the fourth phase in the ball bearing flight.

The reflected pressure was higher than the gas pressure behind the ball bearing. This pressure differential opposed the motion of the ball bearing, accelerating it in the opposite direction, causing a small decrease in velocity. At t = 55.5 μs, the ball bearing velocity had measurably decreased due to the pressure reflection. Recirculation of the gaseous products was observed at the end of the blast tube, where the gases on the sides of the blast tube propagated towards the centre of the tube and began to merge. In the fifth phase (not shown), the recirculated gas products merged and the ball bearing velocity stabilised again. The velocity stayed constant until impact on the witness plate. Impact caused deformation of the aluminium witness plate and the ball bearing velocity rapidly decreased.

Influence of charge length on maximum flight velocity

A graph of maximum ball bearing velocity versus charge mass, grouped by charge diameter, is shown in Figure 23. In general, smaller diameter charges were more effective at driving the ball bearing at low charge masses, as was expected from previous work on aspect ratio effects [10-12]. At a constant charge diameter, the velocity increased non-linearly until a maximum effective charge length (corresponding to a critical aspect ratio) was reached. Based on the Kennedy [13] simplification, this critical *L/D* was proposed to be $\sqrt{3}/2$, as illustrated in Figure 24 where a linearly scaled velocity was plotted against logarithmically scaled aspect ratio (corresponding to charge mass for a constant charge diameter grouping). Ball bearing velocity increase was approximately linear up to the critical aspect ratio. The ball bearing velocity appeared to have increased at a slower rate beyond the critical aspect ratio although the gradient change is gradual. This is particularly evident for the 18 mm to 30 mm diameter charges, where the velocities fall significantly below the linear trendlines shown in Figure 24.

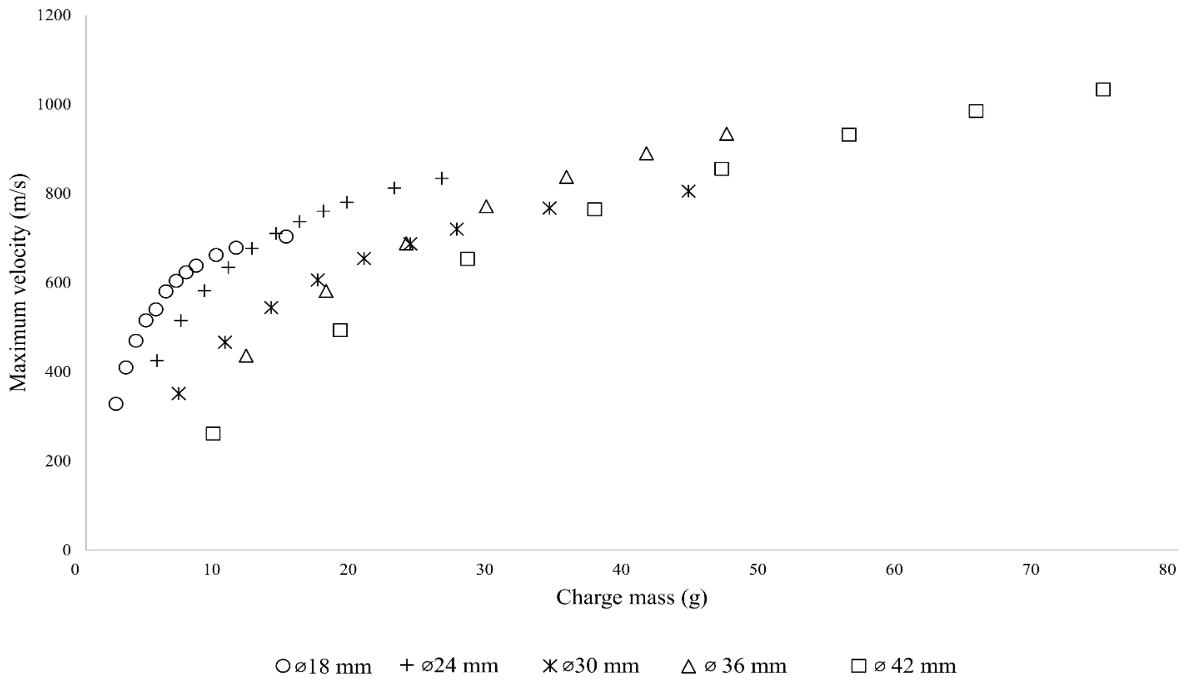

Figure 23: Graph of maximum velocity versus charge mass, grouped by charge diameters.

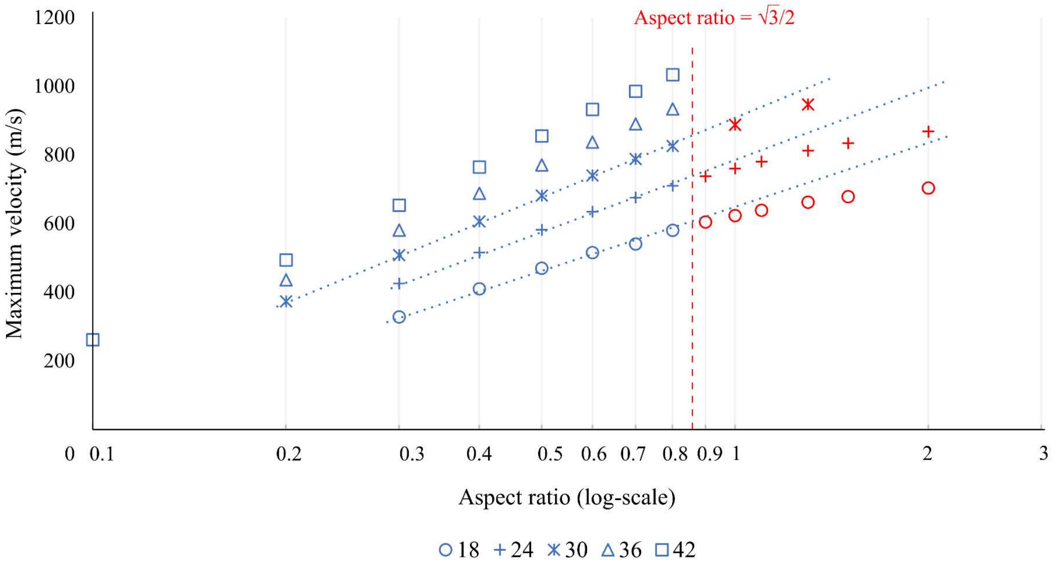

Figure 24: Graph of maximum velocity versus charge aspect ratio (log scale), grouped by charge diameter.

6.5 Influence of explosive charge geometry on ball bearing velocity

Detonation wave propagation and axial velocity (phase 1, prior to contact with ball bearing)

The simulated pressure contour development in the early stages (during the detonation phase, but prior to contact with the ball bearing) for a 72 mm long, 36 mm diameter charge (aspect ratio of 2) is shown in Figure 25. It illustrates the shape of the detonation front as it propagated through the charge. A 3.2 mm line detonation which initiated simultaneously across the length was used in the model. As the detonation proceeded from the initiation point, Figure 25(a) shows (after 0.265 μs) the detonation front expanding both radially and axially as unreacted explosives exist in both directions. In the extreme case, where the thickness of the reaction zone was lower than the charge length, the detonation front would not propagate.

After a short time, the detonation front had expanded to the radial edge of the charge (thereafter generating blast waves in the air propagated radially away from the charge). The detonation front flattened in the central region but was curved at the edges. An example is shown after 0.756 μs in Figure 25 (b). The detonation front continued to propagate, and the front flattened across the full diameter, as shown in Figure 25 (c) after 2.874 μs. For explosive charges that were sufficiently long, the axial expansion and propagation of the detonation front continued until the wave front reached the opposite face. This axially propagating wave is shown in Figure 25d after 4.022 μs.

Detonation wave propagation and blast arrival time

In Figure 19, the effect of charge length on blast arrival time was divided into two zones at $L < 14$ mm and $L > 14$ mm, respectively. The blast arrival time was taken as time from the initiation of detonation until the arrival of the first blast wave. This feature can be explained by the development of the detonation pressure front, shown in Figure 25, for L = 36 mm. The blast arrival time decreased with the increase in charge length with a steeper gradient up to a length of 14 mm because the detonation wave requires a finite length of explosive for its front to have sufficiently expanded (illustrated by the expanding front shown in Figures 25a,b). In zone 2 (in Figure 19), the charge length was sufficient for the detonation front to develop fully. This allowed the detonation front to flatten and attain its maximum detonation velocity. The distance travelled by the blast waves increased with increasing charge length, thus increasing the blast arrival times with increasing charge length in zone 2. Hence, the propagation of the detonation pressure wave supports the trends observed in Figure 19.

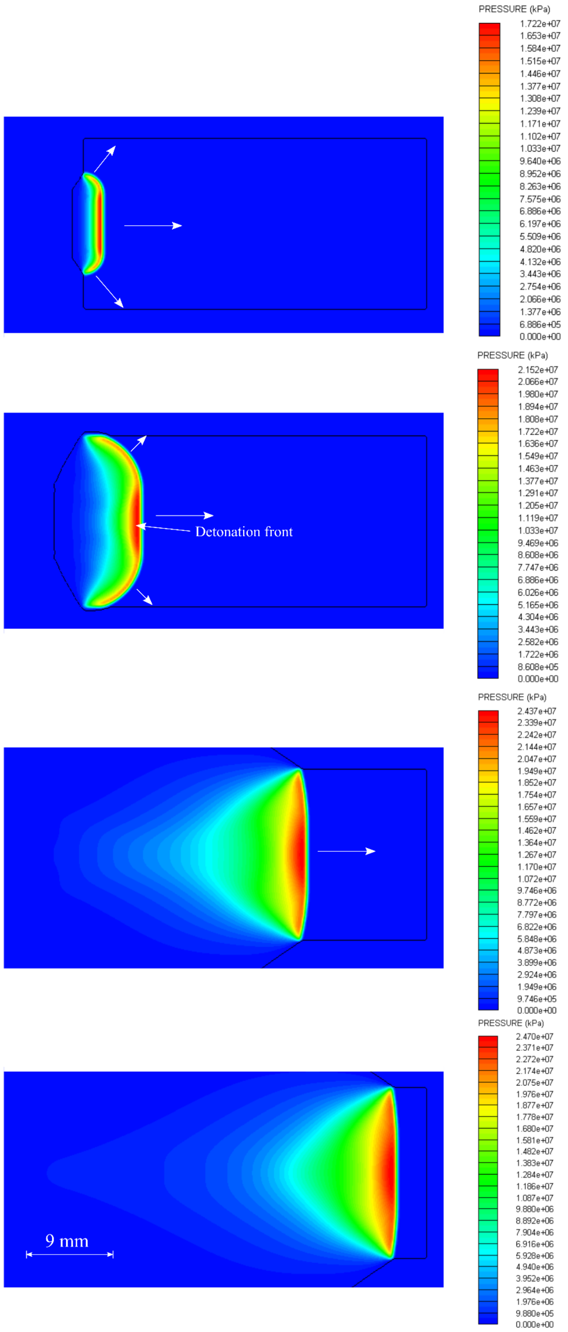

a)

Radial and axial expansion

0.265 µs

b)

Reduced radial expansion

0.746 µs

c)

Axial expansion

0.2874 µs

d)

Continued axial expansion

4.022 µs

Figure 25: Pressure contour development of a Ø 18 mm, *L/D* =2 charge simulated in Autodyn at: a) 0.265 µs, b) 0.756 µs, c) 2.874 and d) 4.022 µs after detonation

Influence of aspect ratio on detonation front characteristics at bearing location

Understanding the detonation pressure can provide insightful explanations of the ball bearing velocities observed experimentally and numerically. The pressure contour during detonation at different times were captured for Ø 18 mm charges at *L/D* = 0.3, *L/D* = 0.8, *L/D* = 2; for Ø 24 mm charges at *L/D* = 0.3, *L/D* = 2 and for Ø 42 mm charges at *L/D* = 0.3 and *L/D* = 0.8. Figure 26 illustrates the detonation pressure profiles immediately prior to contact with the ball bearing.

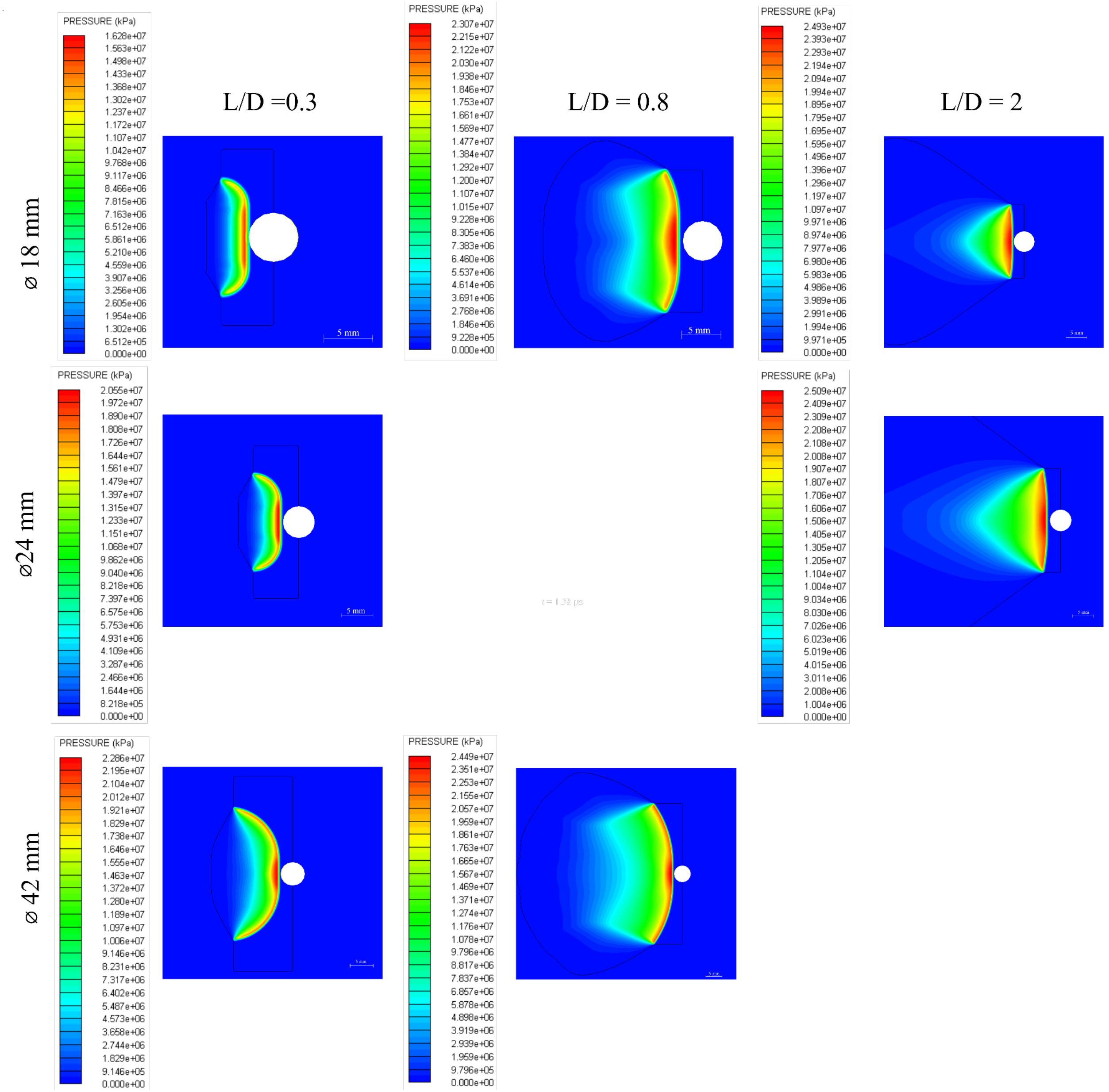

Figure 26: A collection of simulated pressure contours immediately prior contacting the ball bearing

At a constant aspect ratio of 0.3, a more rounded detonation front was observed with the increase in charge diameter because full expansion of the detonation front was not possible prior to contact with the bearing. This rounding was not apparent at an aspect ratio of 2, as the detonation wave had propagated sufficiently that the wave had reached the radial boundary and flattened as it propagated in the axial direction towards the bearing.

For a constant charge diameter of 18 mm, increasing aspect ratio increased the charge length. Here the flattening of the detonation front prior to contact with the bearing can be observed by comparing the shape of the detonation front for *L/D* = 0.8 and *L/D* = 0.3. At *L/D* = 0.8, the radial expansion had reached the radial boundary prior to contact with the bearing, while this had not occurred for *L/D* = 0.3. The increase in aspect ratio for constant charge diameter also implies a larger charge mass, so the increased pressure at the point of contact with the bearing was expected.

There was a distinct shape change in the shape of the gas pressure accumulation within the explosive behind the ball bearing location. At *L/D* = 0.3, the pressure front was relatively thin and flat across the rear of the ball bearing, but was localised to the central third of the charge. As *L/D* increased for a given diameter (i.e. charge length increases), the shape of the pressure front changed. At *L/D* = 0.8 (which is just below the proposed critical aspect ratio of $\sqrt{3}/2$ [12]) the pressure front had rounded, with the radial waves having reached the boundary, and the thickness of the pressure front behind the ball bearing had increased significantly.

Assuming that only the column of pressurised gas with the same diameter as the ball bearing is able to impart forward axial momentum to the bearing, then the increased length of the high pressure column would cause ball bearing velocity to increase at a constant rate with increased charge length for a constant aspect ratio (as observed). This held up to the point where the shape of the pressure column changed. At *L/D* = 2, the shape of the pressure profile was more triangular – the pressure volume behind the ball bearing was more conical at high aspect ratios, and the increase in ball bearing velocity at higher aspect ratios (shown in Figure 24) tapered off. This explanation is consistent with the Kennedy simplification [13].

6.6 Momentum transfer mechanism from charge to bearing

Momentum transfer and damage characteristics at low charge aspect ratios

The simulations showed that charge geometry significantly influenced the detonation pressure profile up to the point of contact with the ball bearing. After this, the presence of the ball bearing significantly altered the pressure propagation through the explosive. Figure 27 shows a sequence of simulated pressure contours from the detonation of a typical cylindrical charge (18 mm diameter, *L/D* = 0.4). The first image shows the pressure front at the point of contact (at 0.65 μs). As time continued, the flat section of the shock pressure front in the centre of the charge was reflected by the ball bearing due to the impendence mismatch, causing a reduction in pressure along the axis of symmetry (shown more clearly after 0.88 μs). Additionally, some of the pressure front off-centre propagated forward and around the ball bearing, causing an accumulation of pressure around the edges of the ball bearing in contact with the charge. This pressure caused a pinching effect on the rear half of the ball bearing.

The curved section of the detonation front (shown after 0.65 μs, Figure 27) continued to propagate radially until it reflected backwards from the explosive-air interface (shown at 1.1 μs). The side reflections merged at the centre of the cylindrical charge (between times of 1.5-3.4 μs), and exerted an additional axial pressure loading behind the ball bearing on the entire rear surface, as demonstrated after 2.0 μs, while some pressure waves moved past the ball bearing and propagated axially forwards, shown clearly at 3.4 μs. The long column of pressure behind the ball bearing imparted significant axial momentum to the bearing, while the pressure flow around the rear surface caused significant plastic deformation.

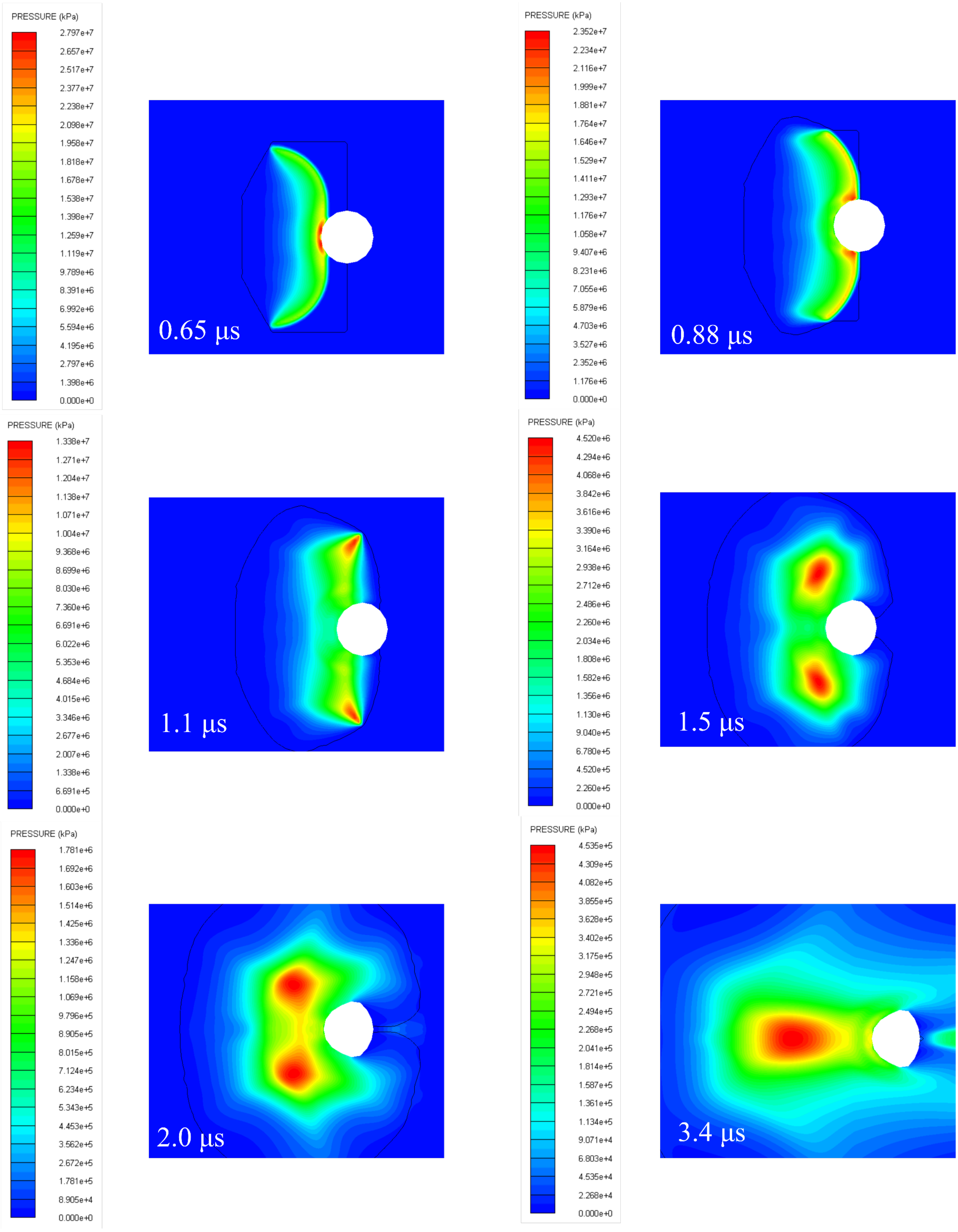

Figure 27 Simulated detonation pressure development with ball bearing interaction for a Ø 18 mm *L*/*D* = 0.4 detonation.

The plastic deformation maps inside the ball bearing, for the corresponding times, are shown in Figure 28. The initial interaction with the pressure wave in the centre caused effective plastic strain accumulation on the rear side of the bearing, with a peak magnitude of 15% after 0.88 µs. Plastic strain continued to accumulate in the rear hemisphere in contact with the charge. The pressures around the bearing face were intense (of the order of several GPa for the first 2 μs). The rear half of the ball bearing appeared sharper (as illustrated in Figure 28 after 2.0 μs), as material was pushed away from the centre and towards the sides of the bearing. The front face of the bearing (away from the charge) flattened slightly due to the movement of material within the bearing from the rear.

Further deformation continued until the strain accumulation approached 30% in the highly deformed sides of the bearing, shown in Figure 27 after 3 μs. The high intensity, short duration, pressure loading caused significant plastic deformation of the ball bearing prior to its inertia-driven motion (the bearing begins to attain significant velocity after 2 μs). Deformation appeared to continue after the bearing gained motion, as shown by comparing the more highly strained bearing profile at 240 μs (just prior to impact) with the map after 3 μs.

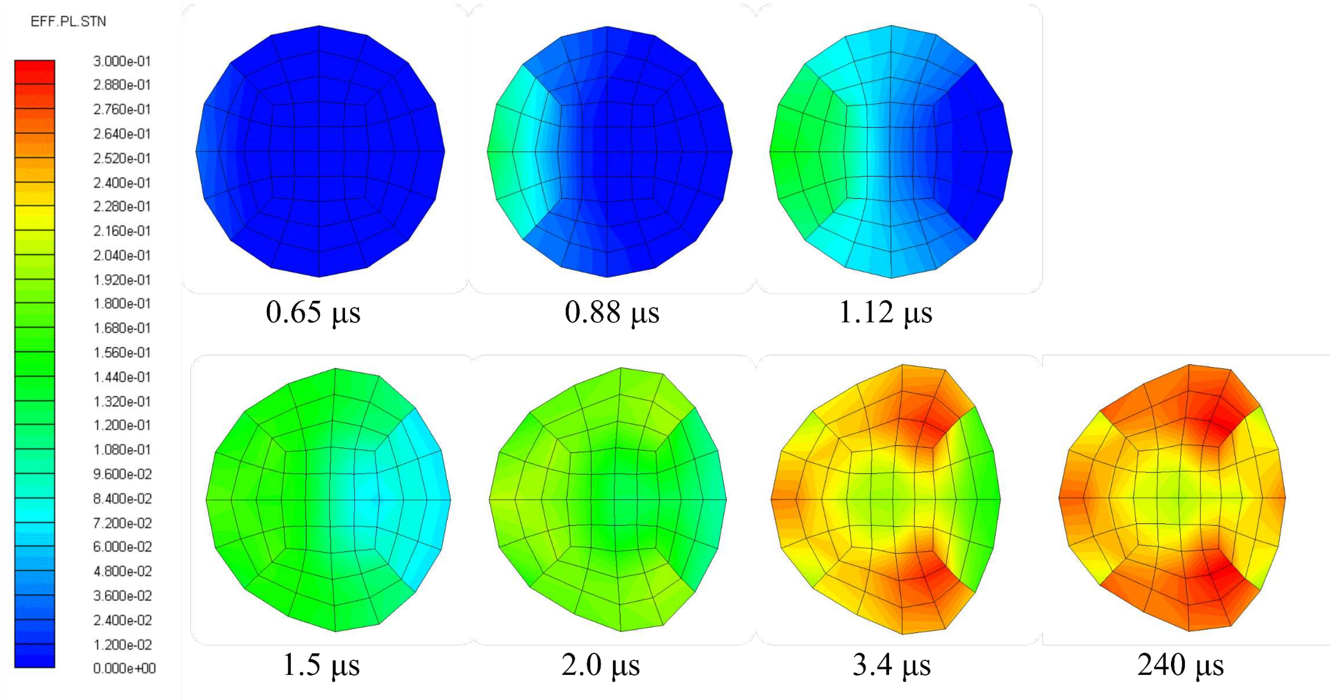

0.65 μs 0.88 μs 1.12 μs

1.5 μs 2.0 μs 3.4 μs 240 μs

Figure 28: Simulated ball bearing accumulated effective plastic strain within the ball bearing, Ø 18 mm, *L/D* = 0.4 detonation.

Momentum transfer and damage characteristics at high charge aspect ratio

As noted previously, the shape of the detonation pressure front at the point of contact with the bearing was influenced by aspect ratio, with high aspect ratio charges producing a detonation pressure contour which was triangular shaped and without curved edges (for example, see *L/D* = 2 in Figure 26). The larger charge mass generated higher magnitude pressures, as might be expected. However, the high aspect ratio also influenced the momentum transfer and ball bearing damage. Figure 29 contains a sequence of simulated pressure contours from the detonation of a typical high aspect ratio charge (18 mm diameter, *L/D* = 2). As the charge was longer, the time sequence starts later at 4.19 μs because it took longer for the detonation front to propagate to the bearing location.

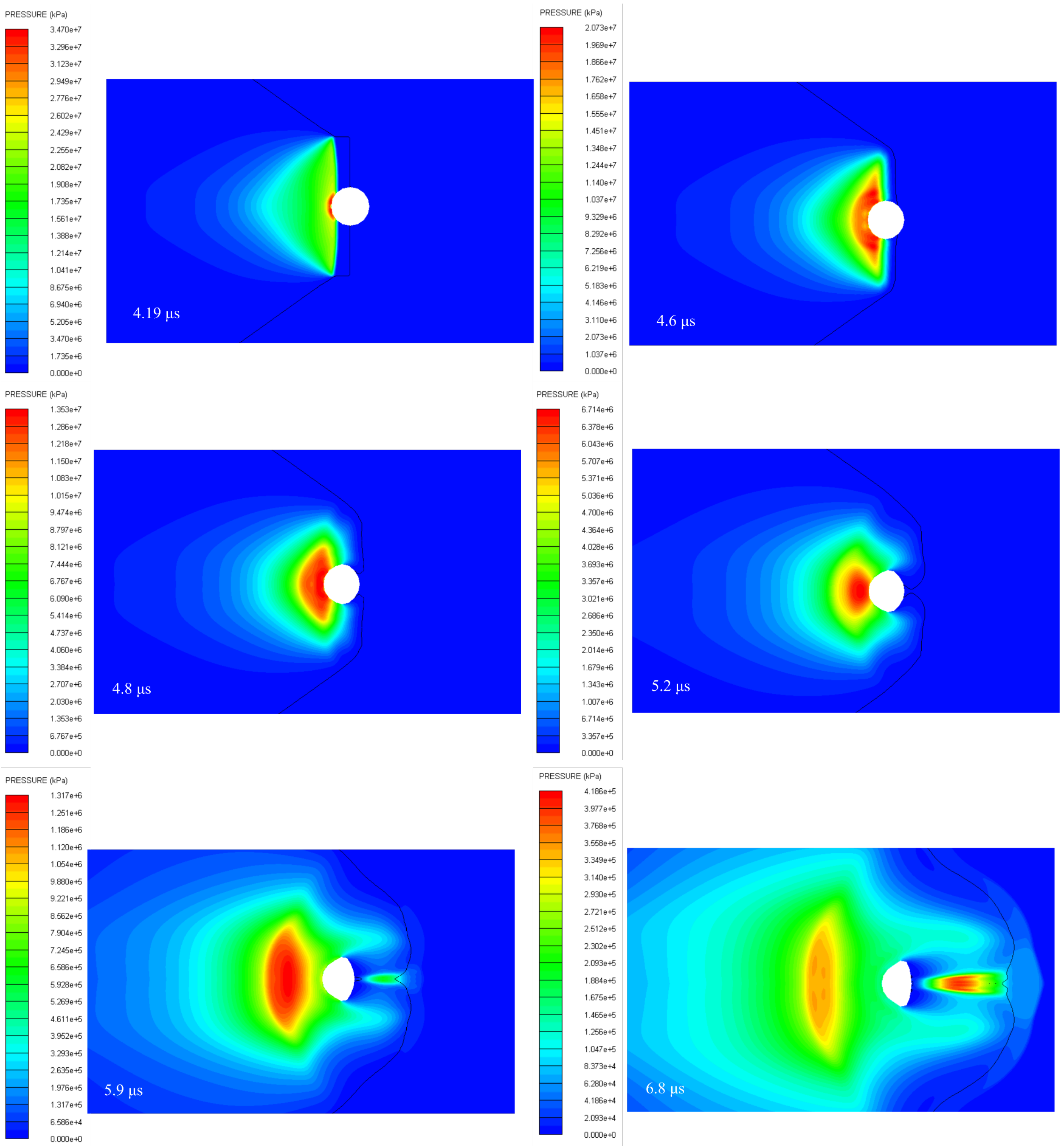

Figure 29: Simulated detonation pressure development with ball bearing interaction for a Ø 18 mm L/D = 2 detonation.

Since the detonation front lacked curved edges, no side reflections were observed. Instead, momentum was only imparted through the initial interaction with the ball bearing and through the hot gas that formed from the reflection of the initial interaction. The lack of recirculation from the edge of the charge resulted in the flatter geometry of the hot gas forming behind the ball bearing, as shown at 6.8 μs. Between 5.2 μs and 6.8 μs, the hot gas behind the ball bearing expanded radially. Triangular type detonation fronts were less effective at imparting momentum to the ball bearing than the column type fronts characteristic of low aspect ratio detonations (such as that shown in Figure 27). The lack of side reflection resulted in a more inefficient mechanism of momentum transfer from charge to bearing, which could have contributed to the lower rate of velocity increase found at higher than critical aspect ratios.

Effective plastic strain plots inside the ball bearing are shown in Figure 30. As before, there was effective plastic strain accumulation on the rear side of the bearing. Plastic strain continued to accumulate in the rear hemisphere, in contact with the charge, while material moved towards the side, as before. The front face of the bearing flattened considerably. Further deformation continued until the strain accumulation approached 55% in the highly deformed sides of the bearing, shown in Figure 27 after 6.8 µs. The front of the bearing was almost completely flattened, compared to the *L/D* = 0.4 case. The strains and deformations were considerably higher, probably due to the higher pressures generated by the larger charge mass. Further investigation is needed to isolate any aspect ratio effects from the charge mass effect.

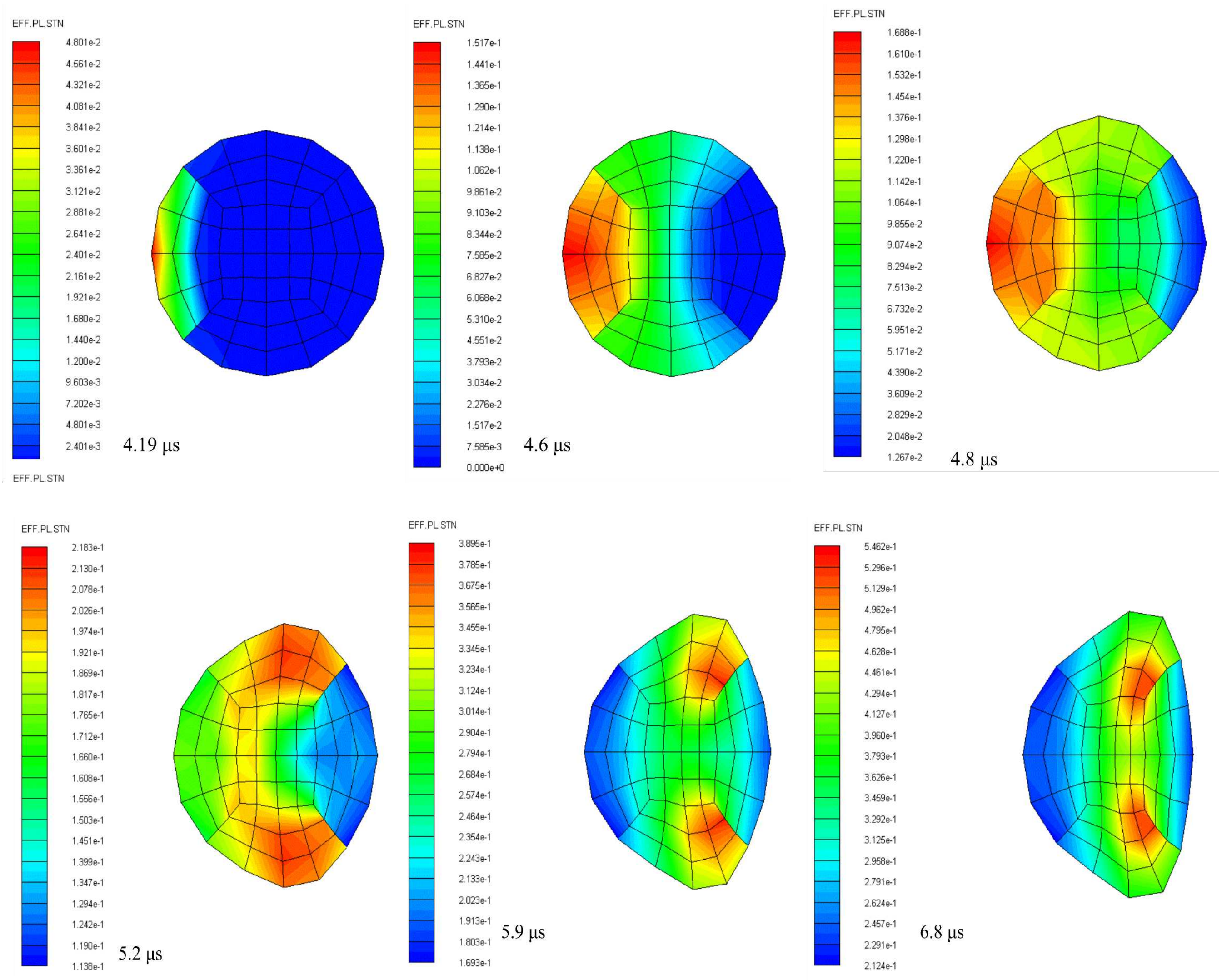

Figure 30: Simulated ball bearing accumulated effective plastic strain within the ball bearing, Ø 18 mm, *L/D* = 2 detonation

6.7 Ball bearing damage and crater depth

From Figure 10, it was evident that the blasted ball bearings exhibited significant flattening to one half of the initially spherical ball. As shown in Figure 31, ball bearings exhibited negligible damage from impact with the witness plates during the gas gun impact tests, so the damage sustained must be due to the blast loading. Interestingly, the simulation results indicated that the rear half of the bearing deformed significantly, appearing to sharpen and push material sideways. Flattening of the front half (away from the charge) was evident in the simulations.

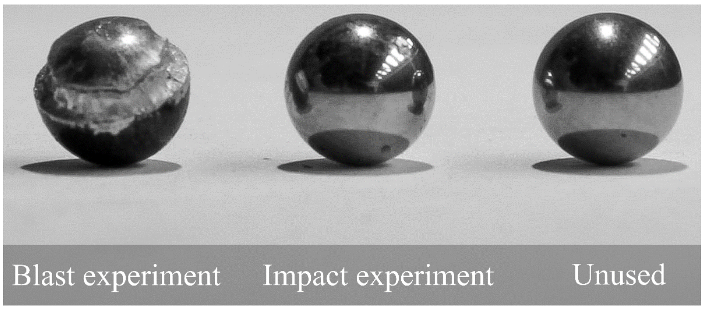

Figure 31 Photograph the ball bearings: after a blast experiment (left), an impact experiment using the gas gun (centre) and an unused ball bearing (right).

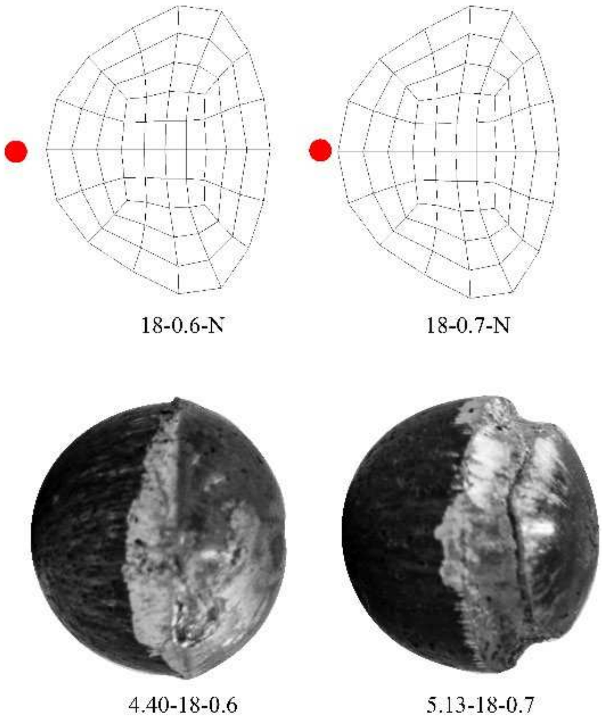

Figure 32 Visual comparison between simulated ball bearing shapes and post-test photographs

A visual comparison between the deformed shape predicted in the computational simulations and that obtained experimentally is presented in Figure 32. The red dot to the left of the deformed shape indicates the rear side (that is, the ball bearing side closest to the charge). The simulated shapes show that the flattened side of the ball bearing is the side facing away from the charge (this could not be determined experimentally as the bearings were retrieved from the floor of the blast chamber) and so the physical ball bearings are oriented to match this. The simulations appeared over-estimated the amount of damage to the bearing, probably as a result of the nominal material properties used. Further details concerning the ball bearing damage assessment are available in Qi et al [43] as the focus of this paper is on the momentum transfer during detonation.

A graph of crater depth versus charge mass is shown in Figure 33, for the experimental and numerical results. Good agreement was observed for detonations up to 6 g PE4. Above 6g, the physical and computational crater depths diverged. The model predicted that crater depth would be unaffected by charge mass above 6g, while the experiment measured craters continued to increase in depth with increasing charge mass. At 10g, the crater depth obtained experimentally was almost twice the numerical prediction. Simulation above 6g also produced significantly more severe bearing deformation (such as that shown in the last image of Figure 30). Projectile shape is known to influence cratering upon impact, so it is likely that the exaggerated flattening of the ball bearing from the simulations will have contributed to the poor correlation with crater depth above 6g.

The maximum deformation observed experimentally was well below the numerical deformation for a 6g detonation. Therefore, for the purpose of impact velocity validation, under the velocity ranges presented in this paper, the influence of bearing deformation was not considered as a major factor. Additional validation between experimental and numerical results of the ball bearing deformation can be found in ref[30] and future publication [43].

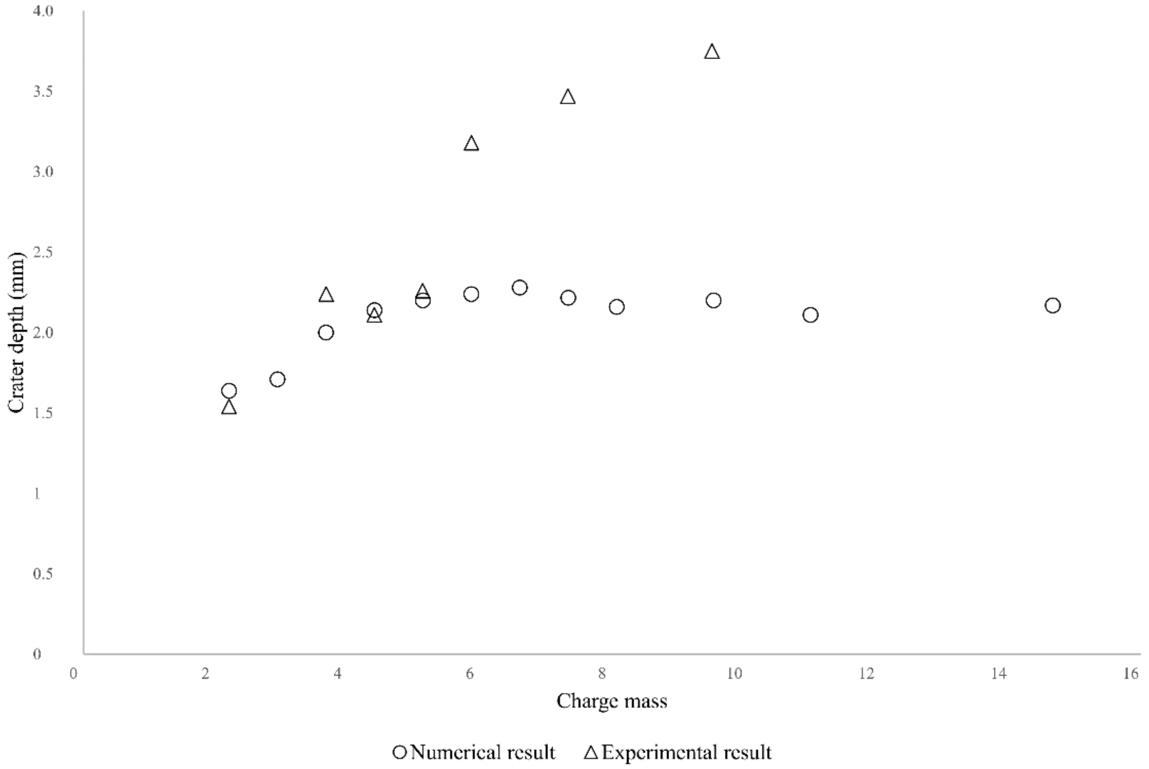

Figure 33 Graph of crater depth versus charge mass results from Ø 18 mm detonations.

Conclusions

A novel experimental technique was developed and implemented to quantify the loading, flight characteristics and damage from a blast-driven ball bearing embedded in a rear detonated cylindrical charge. The ball bearing represented an idealised piece of shrapnel from an improvised explosive device. The axial alignment method used in the blast experiments was successful, allowing more than 80% of the ball bearing impacts to be within 7° from the normal. In general, the simulated results were similar to the experimentally measured values (velocities were within 2% of measured values, although the simulations predicted larger ball bearing deformation and smaller crater depths when the charge mass was above 6g.

Average and impact velocity increased non-linearly with the increase in charge aspect ratio. The rate of increase appeared logarithmic until a critical aspect ratio (proposed to be approximately $\sqrt{3}/2$) and was more gradual thereafter. The HPB measurements implied that impulse imparted by the blast was highly non-uniform and localised in the centre. The simulations confirmed some of the localisation, but not to the extent observed experimentally. The difference was attributed to local irregularities in the fireball development that were not captured by the physics of the simulations, similar to observations by Rigby et al [4].

The simulations showed five phases of the ball bearing flight. During the first phase, the ball bearing acquired axial momentum from the detonation pressure interactions. The geometry of the charge affected detonation profile, which resulted differences in ball bearing velocity. At lower aspect ratios, the momentum transfer to the ball bearing came from a column-type pressure front that was more efficient in transferring momentum. There was no side pressure reflection for charges with higher aspect ratio (above the critical) as the detonation front was flat and the pressure front was triangular. In both cases, the intense pressure flow around the ball bearing caused significant plastic deformation prior to its motion, causing the ball bearings to appear flatter on the front surface and sharper on the rear side.

In the second phase, the shock front overtook the ball bearing and its velocity began to plateau. In the third phase, the ball bearing maintained its constant (maximum) velocity during its flight through the rarefaction expansion waves. During the fourth phase, the reflected blast waves began to interact with the ball bearing, causing a pressure differential that opposed its motion (and a small decrease in velocity). In the fifth phase, the recirculated gas products merged and the ball bearing velocity stabilised again, staying constant until impact on the witness plate.

It is anticipated that this novel detailed investigation into the momentum transfer and flight characteristics of a ball bearing embedded in a rear detonated cylindrical charge will prove useful to blast protection engineers considering the effects of embedded projectiles in IEDs.

Acknowledgements

The authors are grateful to the UCT University Research Committee and the National Research Foundation (NRF) of South Africa for their financial support. Opinions expressed and conclusions arrived at, are those of the authors and are not necessarily to be attributed to the NRF. TThe authors would also like to thank the staff of the Mechanical Engineering workshop at UCT for their assistance in machining the specimens and pendulum parts.

References

1. I. Overton, J. Dathan, C. Winter, J. Whittaker, R. Davies, M. Q. Kaaman, H. Kaaman, Improvised explosive device monitor 2017, *Action on Armed Violence, Tech. Rep.,* 2017.
2. R.G. Stoner, W. Bleakney. The Attenuation of Spherical Shock Waves in Air, *J. Appl Phys*, 19(7):670-678, 1948.
3. M. Held, Impulse method for the blast contour of cylindrical high explosive charges, *Propellants, Explosives, Pyrotechnics*, 24(1):17-26, 1999.
4. S.E. Rigby, A. Tyas, R.J. Curry, G.S. Langdon. Experimental measurement of specific impulse distribution and transient deformation of plates subjected to near-field explosive blasts, *Exper Mech*, 59(2):163-178, 2019.
5. M.M. Ismail, S.G. Murray. Study of the blast waves from the explosion of nonspherical charges, *Propellants, Explosives, Pyrotechnics*, 18: 132-138, 1993.
6. P. Sherkar, J. Shin, A. Whittaker, A. Aref, Influence of charge shape and point of detonation on blast-resistant design, *J Struct Engng*, 142(2): 04015109, 2016.
7. C.Wu, G. Fattori, A. Whittaker, D.J. Oehlers. Investigation of air-blast effects from spherical-and cylindrical-ahaped charges. *Int J. Protective Struct,* 1(3):345–362, 2010.
8. C.Wu, D.J. Oehlers, M. Rebentrost, J. Leach, A.S. Whittaker, Blast testing of ultra-high performance fibre and FRP-retrofitted concrete slabs, *Engng Struct*, 31(9):2060-2069, 2009.
9. W. Xiao, M. Andrae, N. Gebbeken. Effect of charge shape and initiation configuration of explosive cylinders detonating in free air on blast-resistant design*. J Struct Engng* 146.8:04020146, 2020.
10. G. N. Nurick, S. Mahoi, G. S. Langdon, The response of plates subjected to loading arising from the detonation of different shapes of plastic explosive, *Int J Impact Engng*, 89: 102-113, 2016.
11. G.S. Langdon, S.C.K. Yuen, G.S. Nurick, Experimental and numerical studies on the response of quadrangular stiffened plates - Part II: localised blast loading, *Int J Impact Engng*, 31(1): 85-111, 2005.
12. N. Jacob, S.C.K. Yuen, G.N. Nurick, D. Bonorchis, S. Desai, D. Tait, Scaling aspects of quadrangular plates subjected to localised blast loads|-experiments and predictions, *Int J Impact Engng*, 30(8-9): 1179-1208, 2004.
13. J. Kennedy. Gurney energy of explosives: Estimation of the velocity and impulse imparted to driven metal, *Tech. Rep.,* 1970.
14. R.W. Gurney, The initial velocities of fragments from bombs, shell and grenades, Army Ballistic Research Lab Aberdeen Proving Ground Md, *Tech. Rep.,* 1943.
15. V. Balden and G. Nurick, Numerical simulation of the post-failure motion of steel plates subjected to blast loading, *Int J Impact Engng*, vol. 32, no. 1-4, pp. 14–34, 2005

16. Q. Zhang, C. Q. Miao, D. C. Lin, C. H. Bai, Relation of fragment with air shock wave intensity for explosion in a shell, *Int J Impact Engng*, 28(10): 1129-1141, 2003.
17. P. K. Choudha, A. Kumaraswamy, and K. D. Dhote, Parametric study of single confined fragment launch explosive device, *Defence Tech*, 15(2):179–185, 2018.
18. G. Kang, S. Chung Kim Yuen, Response of a structural target to an explosive charge incorporating foreign objects, *Proc 7th Int Conf Struct Engng Mech and Comput (SEMC)*, Cape Town, South Africa, 2019.
19. R.J. Curry, G.S. Langdon, Transient response of steel plates subjected to close proximity explosive detonations in air, *Int J Impact Engng*, 102: 102-116, 2017.
20. *Metallic materials - Tensile testing - Part 1: Method of testing at ambient temperature*, DIN EN 10002-1:2001, 2001.
21. Non-Ferrous Metal Works (SA) (Pty) Ltd, Aluminium 6082, Tech. Rep., 2019.
22. N. Jacob, The effect of stand-off distance on the failure of thin plates subjected to blast loads, *MSc Dissertation*, University of Cape Town, Cape Town, 2005.
23. S.A. Davids, G.S. Langdon, G.N. Nurick, The influence of charge geometry on the response of partially confined right circular stainless steel cylinders subjected to blast loading *Int J Impact Engng*, 108:252-262, 2017.
24. T.J. Cloete, G.N. Nurick, R.N. Palmer, The deformation and shear failure of peripherally clamped centrally supported blast loaded circular plates, *Int J Impact Engng*, 32(1-4): 92-117, 2006.
25. T.J. Cloete, G.N. Nurick, Blast characterization using a ballistic pendulum with a centrally mounted Hopkinson bar, *Int J Protective Struct,* 7(3): 367-388, 2016.
26. P.J. Rae, P.M. Dickson, A review of the mechanism by which exploding bridge-wire detonators function. *Proc. R. Soc.* A 475: 20190120, 2019.
27. J. Silva, L. Li, J.M. Gernand, Reliability analysis for mine blast performance based on delay type and firing time. *Int J Mining Sci Tech,* 28(2): 195-204, 2018.
28. J.A. Zukas, W. Walters, W.P. Walters, *Explosive effects and applications*. Springer Science & Business Media, 2002.
29. R. Qi and T.J. Cloete, A low pressure, supersonic two-stage light gas gun, Work in Progress.
30. R. Qi. The influence of cylindrical charge geometry on the velocity of blast-driven projectiles in one dimension. *MSc dissertation*, University of Cape Town, 2020.
31. A. Tyas, Experimental measurement of pressure loading from near-field blast Events: techniques, findings and future challenges, *Proc 18th Int Conf Exper Mech*, 2(8):471, 2018.
32. L. Schwer, S.E. Rigby. Secondary and height of burst shock reflections: application of afterburning, *Proc. 25th Military Aspects of Blast and Shock*, 2018.
33. S.C.K. Yuen, A. Butler, H. Bornstein, A. Cholet, The influence of orientation of blast loading on quadrangular plates, *Thin-Walled Struct*, 131:827–837, 2018.
34. J. Lee, E.L. Hornig, H.C. Kury, Adiabatic expansion of high explosive, 1968. doi:10.2172/4783904.

35. D Bogosian, M Yokota, SE Rigby, TNT equivalence of C-4 and PE4: a review of traditional sources and recent data, *24th Military Aspects of Blast and Shock*, Nova Scotia, Canada, 2016.
36. G.R. Johnson, A constitutive model and data for materials subjected to large strains, high strain rates, and high temperatures, *Proc. 7th Inf. Sympo. Ballistics*, pp. 541-547, 1983.
37. P. Yibo, W. Gang, Z. Tianxing, P. Shangfeng, R. Yiming, Dynamic mechanical behaviors of 6082-t6 aluminum alloy, *Adv in Mech Engng*, 2013.
38. ANSYS Inc., Ansys Autodyn material library (r18), 2018.
39. L. Rayleigh, Investigation of the character of the equilibrium of an incompressible heavy fluid of variable density, *Proc of the London Mathematical Soc*, 4(1):170–177, 1882.
40. G.I. Taylor GI, The instability of liquid surfaces when accelerated in a direction perpendicular to their planes. II, *Proc Royal Soc of London. Series A– Mathematical & Phys Sci,* 201(1065): 192–196, 1950
41. R.D. Richtmyer, Taylor instability in a shock acceleration of compressible fluids, *Los Alamos Scientific Lab*, N. Mex., 1954.
42. E.E. Meshkov, Instability of the interface of two gases accelerated by a shock wave, *Fluid Dynamics*, 4(5):101–104
43. R Qi, G.S. Langdon, T.J. Cloete, S.C.K. Yuen, Blast-driven ball bearings: flight characteristics and high-rate deformation evolution, In preparation for *DYMAT 2021 13th International conference*.